

RESEARCH ARTICLE

10.1002/2015JD024624

Key Points:

- Persistent weak PMC albedo was found in 60°W–150°W of the SH but not in the NH
- Weak PMC coincides with higher T from MLS and lower modeled ice density
- Weak PMC coincides with warm phases of strong nonmigrating 12 h tides from SABER

Correspondence to:

X. Liu,
liuxiao@htu.edu.cn

Citation:

Liu, X., J. Yue, J. Xu, W. Yuan, J. M. Russell III, M. E. Hervig, and T. Nakamura (2016), Persistent longitudinal variations in 8 years of CIPS/AIM polar mesospheric clouds, *J. Geophys. Res. Atmos.*, 121, 8390–8409, doi:10.1002/2015JD024624.

Received 8 DEC 2015

Accepted 12 JUL 2016

Accepted article online 15 JUL 2016

Published online 28 JUL 2016

Persistent longitudinal variations in 8 years of CIPS/AIM polar mesospheric clouds

Xiao Liu^{1,2}, Jia Yue^{3,4}, Jiayao Xu², Wei Yuan², James M. Russell III³, M. E. Hervig⁵, and Takuji Nakamura⁶

¹Henan Engineering Laboratory for Big Data Statistical Analysis and Optimal Control, School of Mathematics and Information Sciences, Henan Normal University, Xinxiang, China, ²State Key Laboratory of Space Weather, National Space Science Center, Chinese Academy of Sciences, Beijing, China, ³Department of Atmospheric and Planetary Sciences, Hampton University, Hampton, Virginia, USA, ⁴ESSIC, University of Maryland, College Park, Maryland, USA, ⁵GATS Inc., Driggs, Idaho, USA, ⁶National Institute of Polar Research, Tokyo, Japan

Abstract The Cloud Imaging and Particle Size (CIPS) instrument on the Aeronomy of Ice in the Mesosphere (AIM) satellite provides an opportunity to study the longitudinal variation in polar mesospheric cloud (PMC). We examined the longitudinal variation in PMC albedo using 8 years (2007–2014) of observations from the CIPS instrument. The results show that the PMC albedo in the Southern Hemisphere (SH), especially in the latitude band of 80°S–85°S, is persistently low (~65% relative to the rest of the hemisphere) within 60°W to 150°W longitude. In the Northern Hemisphere (NH), however, PMC albedo is found to be relatively zonally asymmetric. Harmonic analyses show that the persistent longitudinal variation in the SH PMC albedo is due to zonal wave numbers 1 through 4 (WN1–WN4) processes with minima in the longitude range of 60°W–150°W. The influence of temperature and H₂O on the longitudinal variation of the PMC albedo is discussed based on results obtained using a simple 0-D PMC model and temperature from the Microwave Limb Sounder (MLS) and the Sounding of the Atmosphere with Broadband Emission Radiometry (SABER) and H₂O from MLS. The modeled region of low ice mass in the SH is generally consistent with that of low PMC albedo seen in CIPS. Tidal analyses using the SABER temperatures indicate that the nonmigrating semidiurnal tides with modes of S0, W1, and E1 might be the main drivers of the persistent longitudinal variations of PMC albedo in the SH. Nonmigrating tides are much weaker in the NH and consistent with the observed lack of longitudinal variability in PMC albedo.

1. Introduction

Polar mesospheric clouds (PMCs) are primarily composed of water ice crystals formed in the summer polar mesopause region [Hervig et al., 2001]. The ice water nature of PMC makes them sensitive to temperature, water vapor, and condensation nuclei [Jensen and Thomas, 1988; Siskind et al., 2005; Karlsson and Rapp, 2006; Rapp and Thomas, 2006]. Thus, PMC is considered a sensitive indicator for detection of global climate change and interhemispheric coupling [Thomas, 1996, 2003; Thomas et al., 2003; Karlsson et al., 2007, 2009; Benze et al., 2012]. The topics, such as the formation of PMC and the temporal and spatial variations of PMC, have received much attention in the community of upper atmospheric studies.

Previous observations have illustrated that PMC varied with time scales from diurnal to decades. Ground-based lidar observations have shown the diurnal and semidiurnal variations in PMCs in the polar regions [e.g., Chu et al., 2003, 2006; Fiedler et al., 2005, 2011]. Numerical modeling studies showed that short period (<10 h) gravity waves destroy visible PMC and long period (>10 h) gravity waves temporarily enhance the brightness of existing PMC. However, both short and long period gravity waves reduce the domain averaged PMC brightness in the long term [Jensen and Thomas, 1994; Chandran et al., 2012]. Using the PMC occurrence frequency data derived from the Spatial Heterodyne Imager for Mesospheric Radicals (SHIMMER) between 50°N and 58°N, Stevens et al. [2009] have revealed the semidiurnal variations of PMC with peaks at 06 LT (local time) and 18 LT. Using the assimilation data and a PMC model, Stevens et al. [2010] found that the migrating diurnal tide controls the diurnal variations of PMC at 69°N. Using the PMC data derived from the Ozone Monitoring Instrument (OMI) on Aura satellite, DeLand et al. [2011] showed that the local time (e.g., diurnal and semidiurnal) variations of the PMC brightness and occurrence frequency are dependent on latitude and cloud brightness.

The 5 day and 27 day variations in PMC have been revealed from various satellite and ground-based observations. The 5 day variations of PMC are anticorrelated to the 5 day planetary wave in temperature at the PMC height (~82–87 km) [e.g., Kirkwood et al., 2002; Merkel et al., 2003; von Savigny et al., 2007; Nielsen et al., 2010; Liu et al., 2015]. Using the observations from Scanning Imaging Absorption Spectrometer for Atmospheric

Chartography (SCIAMACHY) and Solar Backscatter Ultraviolet (SBUV), *Robert et al.* [2010] revealed the 27 day variation in PMC, which is anticorrelated to temperature and solar radiation flux instead of water vapor. Moreover, the 27 day variation of PMC was also studied by *Thomas et al.* [2015], who used the temperature, water vapor, and ice water content (IWC) over 15 PMC seasons measured by Solar Occultation for Ice Experiment (SOFIE) instrument on board the Aeronomy of Ice in the Mesosphere (AIM) satellite.

The seasonal and interannual variations of PMC have been revealed from both ground-based and satellite observations [*Chu et al.*, 2003; *Kirkwood et al.*, 2008; *Fiedler et al.*, 2011; *Siskind et al.*, 2011]. Using 14 year data set of PMC observed by Arctic Lidar Observatory for Middle Atmosphere Research (ALOMAR) (69°N , 16°E) lidar, *Fiedler et al.* [2011] showed that the seasonal averaged PMC altitudes are correlated to both Lyman α radiation and temperature. The ground-based observations of PMC over a period of 43 years (1964–2006) from UK and Denmark exhibited quasi-decade variation, which is anticorrelated with solar cycle variation of solar radiation flux, and a significant increasing trend in faint PMC. However, there is no long-term trend in moderate or bright PMC. This inconsistency may be due to the observing methods [*Kirkwood et al.*, 2008].

Besides the temporal variations of PMC mentioned above, previous observations also showed that PMC and its variations vary with latitude and exhibit hemispheric asymmetry. PMC brightness and occurrence frequency measured by SCIAMACHY, SBUV, and SBUV/2 instruments illustrated that the long-term trends in PMC depend on latitudes. The long-term trends in PMC brightness and occurrence frequency increase significantly with the increasing latitudes [*DeLand et al.*, 2007; *Shettle et al.*, 2009]. It should be noted that the measured PMC brightness and occurrence frequency and their long-term trend might be influenced by many factors such as instruments, sampling time, latitude, and decade interval [*Stevens et al.*, 2007; *DeLand and Thomas*, 2015]. The interhemispheric asymmetry of PMC has been studied by *Hervig et al.* [2013] using the PMC data measured by the SOFIE instrument on board the AIM satellite. They showed that the higher PMC occurrence frequency is due to the lower temperature in the Northern Hemisphere (NH) than in the Southern Hemisphere (SH). Subsequently, *Hervig et al.* [2015] showed that PMC variability in the southern polar region is primarily controlled by temperature, while a combination of temperature and water vapor is responsible for the PMC variability in the northern polar region.

Ground-based observations of PMC illustrated that there is either negative or no correlation between the PMC brightness and gravity wave strength [*Gerrard et al.*, 1998, 2002; *Thayer et al.*, 2003; *Innis et al.*, 2008; *Chu et al.*, 2009; *Liu et al.*, 2014]. Using the PMC albedo imaged by the Cloud Imaging and Particle Size (CIPS) instrument during the 2007 and 2008 PMC seasons (from May to August in the northern polar region), *Chandran et al.* [2010] showed that the different correlations between PMC occurrence and gravity wave activity at different locations might be resulted from the local environment differences in the background temperature and local gravity wave activity at the PMC height. In contrast, *DeLand et al.* [2011] showed that longitudinal variations in the PMC albedo from OMI are much smaller than the local time variations. *DeLand et al.* [2011] ascribed this difference to the different date coverage in one PMC season and different latitude bands. The results reported in *DeLand et al.* [2011] were based on a relatively small latitude band (2° in latitude), whereas *Chandran et al.* [2010] used a 10° latitude band (70° – 80°S) in each hemisphere. Thus, further studies should be performed to study the longitudinal variations of PMC using data with longer temporal coverage.

The differences in the background temperature may be related to local time and longitudes and thus tides in the mesosphere and lower thermosphere (MLT). Both ground-based and satellite observations in the MLT region over the Antarctic and Arctic revealed the semidiurnal nonmigrating tides in both the zonal and meridional winds. Using four ground-based radar observations over Antarctic, *Murphy et al.* [2003, 2006] found the westward propagating wave number 1 (W1) nonmigrating semidiurnal tide in the mesosphere and lower thermosphere over Antarctica. Using 12 years horizontal wind data from Scott Base MF radar and the Halley Super Dual Auroral Radar Network (SuperDARN) radar, *Hibbins et al.* [2010] also found strong nonmigrating semidiurnal tide during summer Antarctic. Using the wind data observed by TIMED Doppler Interferometer (TIDI) on board Thermosphere, Ionosphere, Mesosphere, Energetics, and Dynamics (TIMED) satellite, *Iimura et al.* [2009, 2010] illustrated the existence of the nonmigrating semidiurnal tides with modes of W1, W3 (westward propagating with zonal wave number 3), S0, and E1 (eastward propagating with zonal wave number 1) in Antarctic and with modes of W1, W3, and S0 in the Arctic. A full diurnal cycle Fe lidar at Antarctic detected substantial diurnal and semidiurnal tides in temperature [*Lübken et al.*, 2011]. The nonmigrating components of these tides should influence the longitudinal variations of temperature and thus the PMC albedo.

The focus of this paper is to explore the persistent longitudinal variations of PMC albedo imaged by CIPS over the past eight PMC seasons (2007–2014) in both the northern and southern polar regions. The possible mechanism, which is responsible for the longitudinal variations of PMC albedo, will also be explored. Then the temperature and water vapor measured by two satellites and a zero-dimensional (0-D) PMC model developed by *Hervig et al.* [2009] (see the Appendix A for details) are employed to see their influences on the longitudinal variations of PMC.

The remainder of this paper is organized as follows. In section 2, we present the data sets including PMC albedos observed by CIPS, temperature from Sounding of the Atmosphere with Broadband Emission Radiometry (SABER), and temperature and H₂O from Microwave Limb Sounder (MLS) on Aura satellite. In section 3 we present the longitudinal variations of the PMC albedo over the past eight PMC seasons covering both hemispheric polar regions. The possible influences of temperature and H₂O on the PMC albedo will be discussed in section 4. In addition the nonmigrating tides and their influences on PMC albedo will be analyzed using SABER data and presented in section 4. The summary and conclusions are given in section 5. Finally, the 0-D model and the tidal extraction method are described in two appendices, respectively.

2. Data Sets

2.1. CIPS PMC Albedo Images

The AIM satellite was launched into a Sun-synchronous near-circular (600 km altitude) polar orbit on 25 April 2007 [*Russell et al.*, 2009] to study the formation, morphology, and variation of PMC and its relationship to the summer polar mesospheric environment. The CIPS/AIM instrument is one of two instruments on board AIM designed to characterize PMC. CIPS is a wide panoramic UV nadir imager operating at 265 nm with a field of view 120° (along orbit track) by 80° (cross orbit track). Each scene covers a spatial range of approximately 2000 km (along orbit track) by 1000 km (across orbit track) [*Bailey et al.*, 2009; *McClintock et al.*, 2009; *Rusch et al.*, 2009]. The local time (LT) ranges from 12 LT to 24 LT in the northern polar region and from 0 LT to 12 LT in the southern polar region, respectively [see *Lumpe et al.*, 2013, Figure 4]. There are 27 CIPS albedo scenes, which make up one orbit strip. Then ~15 orbit strips in each day are combined into a single image called the “daily daisy,” which covers the entire polar cap region (~55°–87°). The horizontal spatial resolution of the daily PMC albedo image is 5 km × 5 km [*Lumpe et al.*, 2013].

This study uses the daily daisy PMC albedo data (Version 4.20, Level 3a). A detailed description of the albedo retrieval algorithms and validations can be found in previous studies [e.g., *McClintock et al.*, 2009; *Rusch et al.*, 2009; *Lumpe et al.*, 2013].

2.2. MLS Temperature and H₂O

The EOS (Earth Observation System) Aura satellite was launched into a Sun-synchronous polar orbit on 15 July 2004. A detailed description of the Aura satellite and data validation can be found in *Schoeberl et al.* [2006]. The Microwave Limb Sounder (MLS) on board Aura measured temperature, H₂O, and other species. Its LT varies with latitude and ranges from 03 LT to 12 LT in the northern polar region and from 13 LT to 24 LT in the southern polar region. MLS measurements (both temperature and H₂O) in the upper mesosphere have vertical resolution of about 13 km. The MLS/Aura temperature uncertainty increases with height and is about 3 K at the PMC layer altitude (0.00464 hPa or 84 km) [*Schwartz et al.*, 2008].

The MLS/Aura H₂O is scientifically useful in the pressure range of 316 hPa to 0.002 hPa. The uncertainty of MLS H₂O is about 1.5 ppmv (1.1 ppmv) in the pressure level of 0.002 hPa (0.01 hPa) [*Lambert et al.*, 2007, Table 2]. According to the PMC height of ~84 km revealed by *Russell et al.* [2010] and *Hervig et al.* [2013] and similar to *Rong et al.* [2012, 2014] and *Russell et al.* [2014], the MLS temperature and H₂O data at the pressure layer of 0.0046 hPa (~84 km) are used to represent the temperature and H₂O at the PMC layer.

This work uses the MLS/Aura temperature and H₂O along with a simple PMC model (see Appendix A), to study their influences on the PMC albedos. Then the output ice mass density and its longitudinal variations will be compared with the PMC albedos imaged by CIPS.

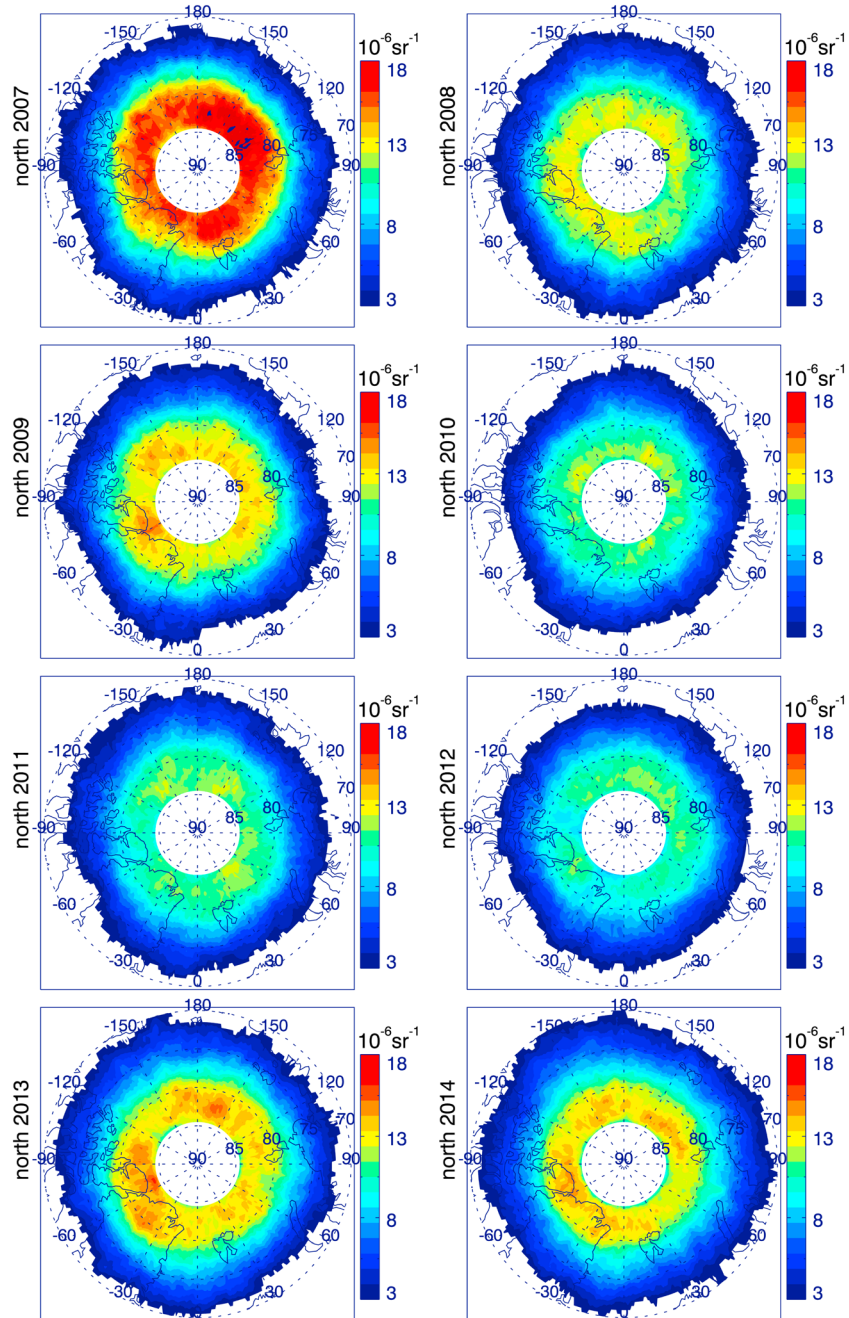


Figure 1. Seasonal (May–August) averages of PMC albedos observed by CIPS in the northern polar region from 2007 to 2014.

2.3. SABER/TIMED Temperature

The TIMED satellite was launched into a 625 km, 74.1° inclined orbit on 7 December 2001. The SABER instrument on board the TIMED satellite measures temperature and other composition profiles [Russell *et al.*, 1999]. The TIMED orbit slowly precesses and takes ~60 days to cover 24 h LT. There are 3 to 5 h of missing data around noon to avoid viewing the Sun directly [Zhu *et al.*, 2005]. The SABER latitude coverage is from 53° in one hemisphere to 83° in the other alternating every ~60 days. The SABER temperature covers the summer polar region (60°N/S–80°N/S) over half of the PMC seasons and can be used to analyze the tidal mode [Merkel *et al.*, 2008]. This work uses SABER temperature data (V2.0, Level 2a) to explore the relationship between nonmigrating tides in temperature and the longitudinal variations of PMC.

3. PMC Over Polar Regions

3.1. Persistent Longitudinal Variation in PMC Albedo

To explore the persistent longitudinal variation in the PMC albedo, Figure 1 shows the seasonal averaged PMC albedos in the northern polar region over the past eight PMC seasons (2007–2014). The seasonal averaged albedos were obtained by averaging the daily daisy PMC albedo over each PMC season. The PMC season in the northern polar region includes May–August. We note that the seasonal averaged PMC albedo eliminates the influences from planetary wave, gravity wave, etc. After eliminating these influences, the persistent longitudinal variation is retained. From Figure 1 we can see that although there is longitudinal variation in the seasonal averaged PMC albedo at latitudes greater than 80°N, the longitude range of low and/or high PMC albedo varies from one season to another. For example, in 2007, the PMC albedo is fairly zonal asymmetry. In 2008, the region of low PMC albedo is of 15°E–90°E. In 2009, the regions of low PMC albedo are of 90°W–120°W and 30°W–40°E.

Similar to that in the northern polar region, Figure 2 shows the seasonal averaged PMC albedos in the southern polar region over the past eight PMC seasons. The PMC season in the southern polar region includes November–February. From Figure 2 we can see that there is always a region (60°W–150°W) in the latitude band of 80°S–85°S where the PMC albedo was lower than other longitudes. Specifically, we listed the longitude range of low PMC albedo of 60–85% lower than the rest of hemisphere: 60°W–150°W during SH PMC seasons of 2007–2008, 2008–2009, 2009–2010, and 2011–2012; 90°W–150°W during SH PMC season of 2010–2011; 15°W–45°W and 60°W–160°W during SH PMC season of 2012–2013; 60°W–120°W and 120°E–150°E during SH PMC season of 2013–2014; 60°W–120°W and 60°E–120°E during SH PMC season of 2014–2015. This shows that there is always a region of low PMC albedo although the seasonal averaged PMC albedo varies from one year to another.

The above analyses show the persistent longitudinal variations of PMC in each PMC season. For a truly persistent feature, it should still be able to see the corresponding behavior using a fixed time window during the core of the season, which then reduces the impact of factors such as interhemispheric coupling (which tends to impact the start time of the season). Thus, we averaged the daily daisies over a time period of 10 days. The SH PMC season of 2009–2010 is taken as an example to illustrate the longitudinal variation in a shorter time scale. This average procedure retains the longitudinal variation in a shorter time scale (10 days) but eliminates the quasi 2 day waves, 5 day wave, and gravity waves. Figure 3 shows the 10 days average of the daily daisies from 22 November 2009 to 19 February 2010. The time interval of performing average is labeled in each panel. From Figure 3, we can find that the magnitude of albedo achieves its maximum in the middle January 2010 and then diminishes as the end of February 2010. There is always a region (60°W–150°W) having low albedo even for the shorter time scale averages. This indicates that the region of low albedo is a persistent feature throughout the PMC season. It should be noted that from 2007 to 2014, the longitude range of low albedo varies from one year to another (Figure 2). In each PMC season (Figure 3), the longitude range of low albedo varies from one time interval to another. Thus, the variability of the longitude range of lower albedo over different time scale is overlaid on the persistent feature.

To explore the persistent longitudinal variations in PMC albedo over the 8 years, the following normalization process was performed on the seasonal averaged PMC albedo. First, the mean albedo of each PMC season was calculated by averaging the zonal mean albedo over the latitude band of 60°N/S–85°N/S. Second, the normalized seasonal averaged albedo was obtained by dividing the seasonal averaged albedo by the corresponding mean albedo of each PMC season. This normalization procedure removes the year-to-year variability in PMC albedo and retains the latitudinal and longitudinal features of the PMC albedo. Finally, we obtain the average of the normalized albedo over the eight seasons. Now the eight seasons' average of PMC albedo can represent the persistent longitudinal variations of PMC albedo, which is the focus of this work.

Figure 4 shows the averages of the normalized PMC albedo over the eight PMC seasons in the northern (Figure 4a) and southern (Figure 4b) polar regions, respectively. From Figure 4, we see that the eight seasons averages of the normalized PMC albedos in the northern polar region (Figure 4a) increased with latitude from 65°N to 85°N and did not exhibit obvious longitudinal variations.

In contrast, the normalized PMC albedos in the southern polar region have a region with an apparently low albedo (~65% relative to the rest of the hemisphere) in the longitude range of 60°W–150°W and in the

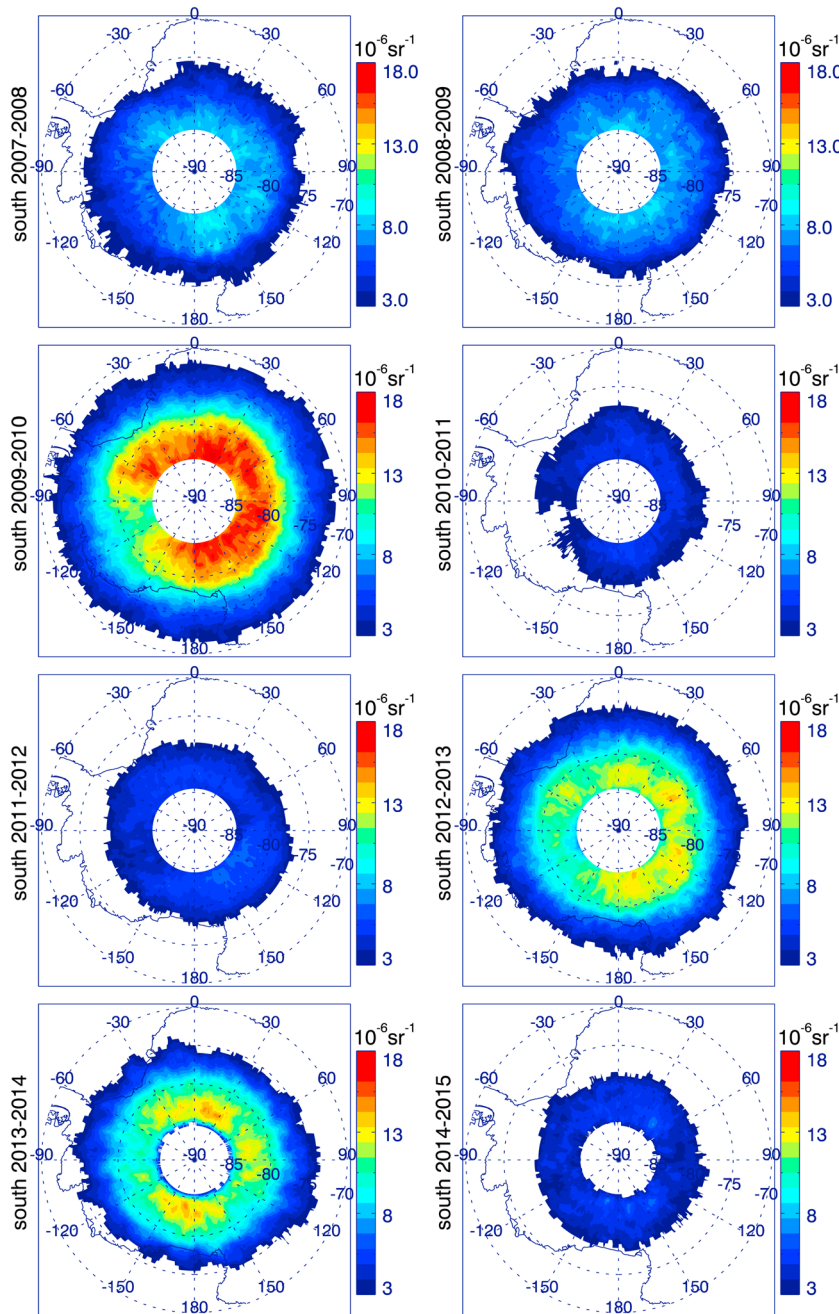


Figure 2. Seasonal (November–February) averages of PMC albedos observed by CIPS in the southern polar region from 2007 to 2014.

latitude range of 80°S to 85°S. This appears to be a persistent longitudinal feature in the PMC albedo and can be confirmed from the longitudinal variations of PMC albedo shown Figure 2. Figure 2 has illustrated that although the PMC albedo exhibits year-to-year variability, the region of low PMC albedo does not vary significantly and mostly in the longitude range of 60°W–150°W at latitudes higher than 80°S. The 2008–2009 SH PMC season is taken as an example to compare with the result of *Chandran et al.* [2010]. Since the albedo decreases sharply from 80°S to 70°S, the longitudinal variation of PMC in the latitude band of 70°S–80°S is not as clear as that in the latitude band of 80°S–85°S. During the 2008–2009 SH PMC season, the seasonal averaged PMC in the latitude band of 80°S–85°S is low in the longitude range of 60°W–120°W, whereas the PMC in the latitude around 75°S–80°S is low in the longitude range of 0°–60°W and 90°W–180°W. This

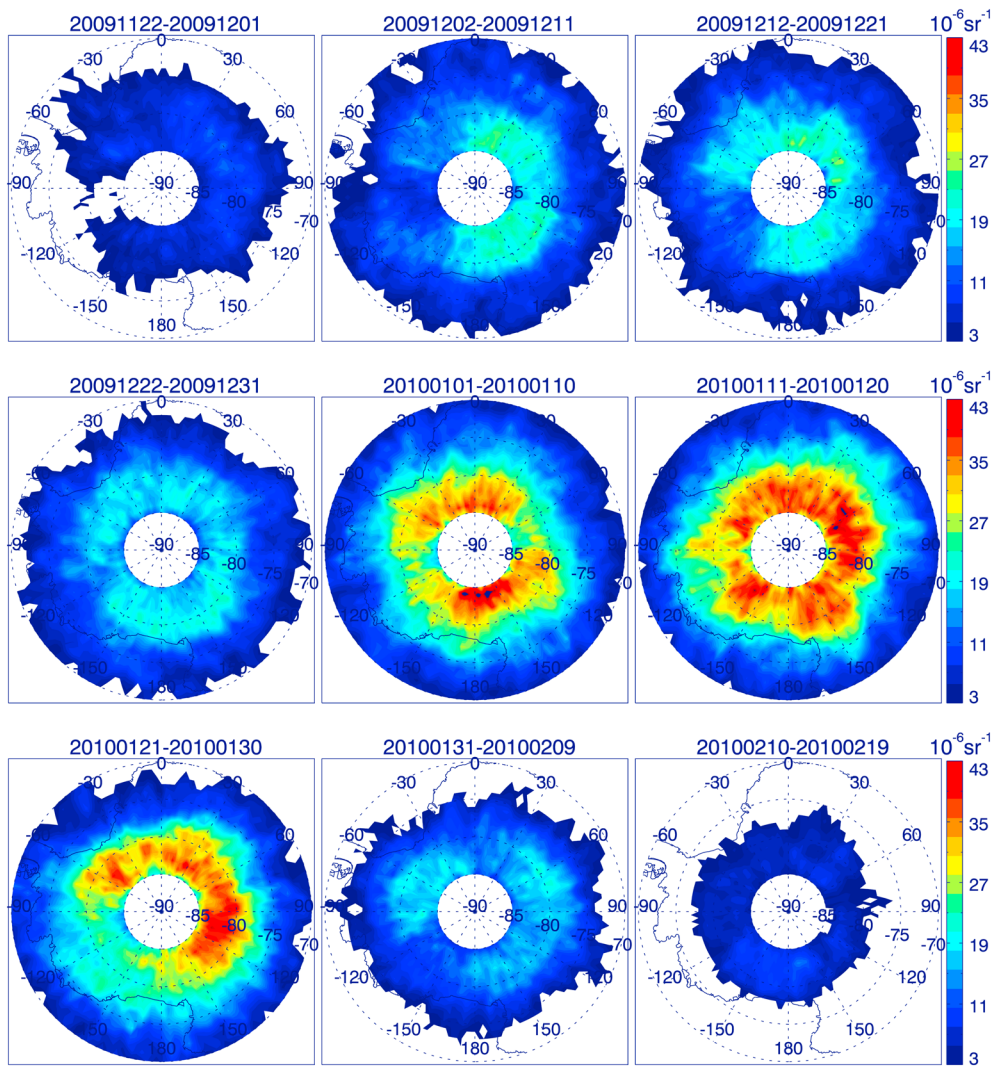


Figure 3. The 10 day average of the daily daisies in the southern polar region from 22 November 2009 to 19 February 2010. The time (YYYYMMDD) interval of performing average is labeled in each panel.

is, in general, consistent with longitude range of 30°E–120°W where PMC occurrence is lower [Chandran *et al.*, 2010, Figure 7d]. However, this does not coincide with the no statistical significant longitudinal variation of PMC albedo from OMI [DeLand *et al.*, 2011]. The zonal wave number components will be analyzed in detail by harmonic analysis in section 3.2.

The latitudinal variation of the PMC albedo shown in Figure 4 also illustrates that the PMC albedo increases with increasing latitude from 70°N/S to 85°N/S and is strongest in the latitude range of 80°N/S–85°N/S. The region with an obvious weaker PMC albedo (Figure 4b) is also in the latitude range of 80°S–85°S where the PMC albedo is strong in general. Thus, the longitude region of the weak albedo can be detected easily in the latitude range of 80°S–85°S. In contrast, the longitudinal variations of albedo are not visible at latitudes lower than 80°N/S and should be examined by harmonic analysis. In section 3.2, we perform harmonic fitting to get more quantitative information for the PMC albedo longitudinal features.

3.2. Zonal Wave Number Dependence of PMC Albedo

To show the persistent longitudinal variation of PMC albedo more clearly, in Figure 5 there are plotted the fluctuations of the eight PMC seasons' averages of the normalized PMC albedos at three representative latitudes (83°N/S, 80°N/S, 75°N/S) and their harmonic fitting results with WN1 to WN4. The fluctuation is

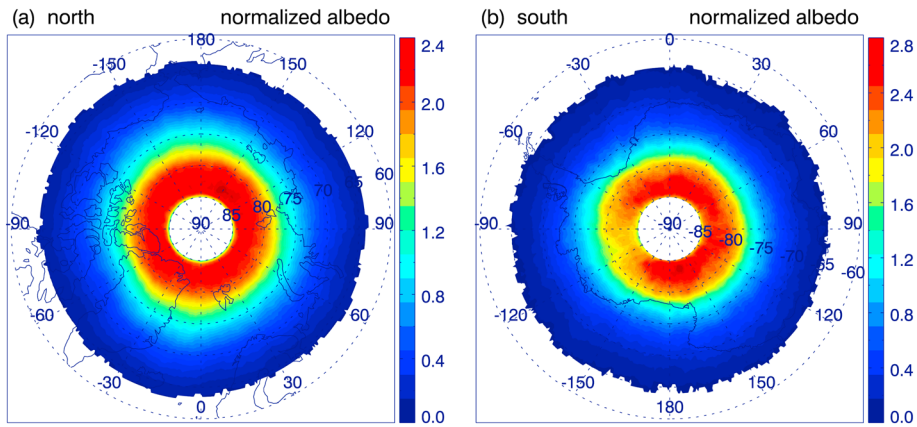


Figure 4. The eight PMC seasons (2007–2014) averages of the normalized PMC albedos observed by CIPS in the (a) northern and (b) southern polar regions. The ranges of the two color bars are slightly different. The normalization process has been described in the text.

defined by the eight PMC seasons' averages of the normalized PMC albedos after subtracting the zonal means normalized albedo and then multiplied by a factor of 100. The reason for choosing these latitudes is that the 83° N/S is the latitude where the albedo peaked, 80°N/S is the latitude where the albedo began to decrease, and 75° N/S is the latitude where the PMC still exists but is much lower than that at 83°N/S and 80°N/S.

From Figures 5a–5c, we can see that WN1 was the strongest among the four wave numbers at 83°N. WN1 and WN2 are equal to one another and stronger than WN3 and WN4 at 80°N. However, at 75°N, among the four wave numbers, WN1 is the weakest, WN2 is the strongest, and WN3 is equal to WN4. From Figures 5d–5f, we

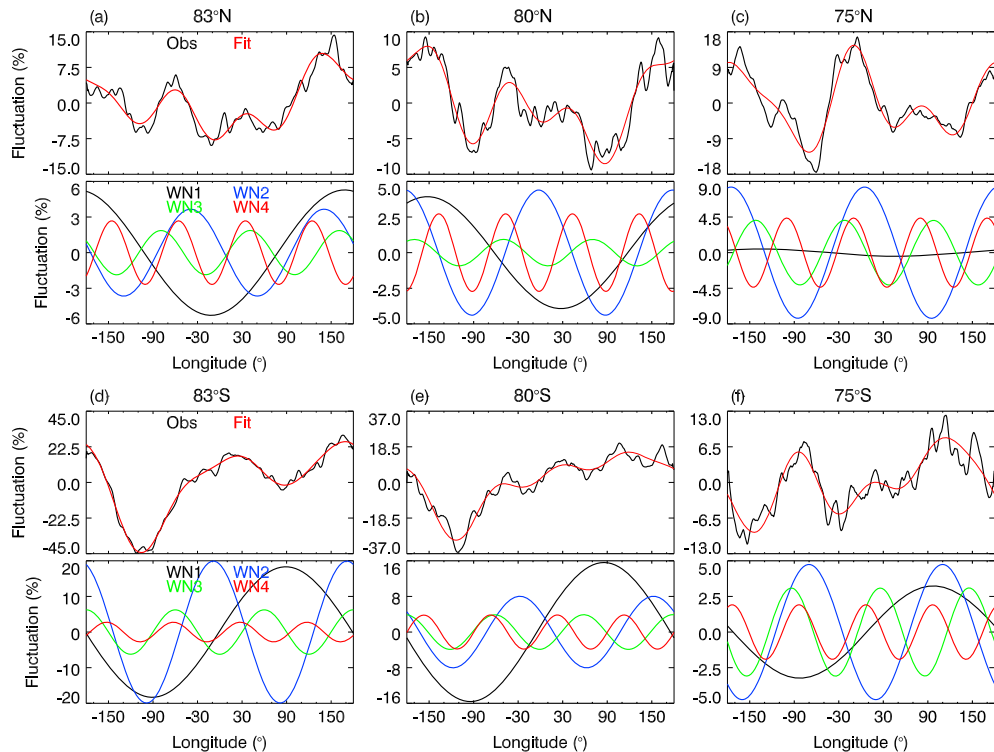


Figure 5. Fluctuations of the eight PMC seasons averages of PMC albedos shown in Figure 4 (black line of the upper plot of each panel) and their fitting results with zonal wave numbers of 1–4 (red line of the upper plot of each panel) at latitudes of (a, d) 83°N/S, (b, e) 80°N/S, and (c, f) 75°N/S in the northern (upper plots of Figures 5a–5c) and southern (upper plots of Figures 5d–5f) polar regions. The fitting results of zonal wave numbers 1 (WN1, black), 2 (WN2, blue), 3 (WN3, green), and 4 (WN4, red) are shown in the corresponding lower plots of each panel.

can see that WN1 and WN2 are equal to one another and are stronger than WN3 and WN4 at 83°S. WN1 is the strongest at 80°S. WN1, WN3, and WN4 have equivalent magnitudes and are weaker than WN2 at 75°S. In summary, WN1 is prominent at 83°N/S and 80°N/S, while WN2 is prominent at 75°N/S. This illustrates that the relative magnitudes of PMC albedo zonal wave numbers are latitude dependent. WN1 and WN2 are much stronger in magnitude at 83°S and 80°S than at 83°N and 80°N.

Now, we explain the region of the weak PMC albedo in the southern polar region (Figure 4b) in terms of zonal wave numbers. The low PMC albedo is formed due to all the four wave numbers having minima in the longitude range of 60°W to 150°W at 83°S and 80°S (the lower plots of Figures 5d and 5e). In contrast, minima of WN1 to WN4 were not exactly in the same longitude range in the northern polar region. Consequently, the cancellations among the four wave numbers result in no region of weak PMC albedo in the northern polar region.

The analyses in this section illustrate that the relative magnitudes of zonal wave numbers are latitude dependent. Moreover, the magnitudes and phase matches of different zonal wave numbers determine the longitudinal variations of albedo.

3.3. Seasonal Dependence and Independence of the PMC Albedo

The zonal wave number dependency of the persistent longitudinal variations in the eight PMC seasons averages of the normalized PMC albedo has been analyzed in the last section. It is reasonable to speculate that there should be a persistent feature in PMC albedo, which does not depend on PMC seasons, so that they can produce the persistent features in the eight PMC seasons averages of the normalized PMC albedo. Thus, the focus of this section is to show the annual dependent and independent of the zonal wave numbers of the PMC albedo in each PMC season. Figure 6 shows the amplitudes and phases of WN1–WN4 in each of the PMC seasonal averaged albedo (left two plots of each panel) and their eight PMC seasons averages (right two plots of each panel) at latitudes of 83°N/S, 80°N/S, and 75°N/S.

First, we focus on the latitudes of 83°N/S and 80°N/S, where the PMC albedo is strong. From Figures 6a to 6c, we can find that although the amplitude of WN1 is the strongest one during most years at 80°N and 83°N (a1, a2, c1, and c2), the phases of WN1 vary from -130° to 180° during the eight PMC seasons (a3, a4, c3, and c4). The relative magnitudes of the amplitudes of WN2–WN4 vary from year to year and do not have wave number preference. The large year-to-year variability of the phase of WN1 and no preference of higher wave numbers would be responsible for the zonally asymmetry in the eight PMC seasons averaged PMC albedo in the northern polar region (Figure 4a). In contrast, at 83°S and 80°S the amplitudes of WN1 and WN2 are stronger than those of WN3 and WN4 during most years (Figures 6b and 6d). The phase of WN1 (WN2) is stable at around 90° (-30°) from year 2007 to 2014 except for the 80°S in the year 2014. Thus, the minimum of WN1 (WN2) locates at around -90° (-120° and 60°). The combination of WN1 and WN2 could produce the weak PMC albedo in the longitude range of 60°W–150°W in the southern polar region (shown in Figure 4b).

Second, we focus on the latitude of 75°N/S, where the PMC albedos are weaker than those at the latitudes of 83°N/S and 80°N/S. The longitudinal variations of PMC albedos are not easy to be visible in Figure 4 but can be seen in Figures 5c and 5f. At 75°N and among WN1–WN4, the amplitude of WN2 (WN1) is the strongest (weakest) one. The phase of WN2 is stable at around 0° during the eight PMC seasons and produces the peaks at around 0° and the troughs at around 90°E/W as shown in Figure 4c. At 75°S, the amplitude of WN2 is slightly stronger than that of WN1, WN3, and WN4. Although the standard deviation of WN2 phase is slightly larger (Figure 6f4), the phase of WN2 is relative stable from 2010 to 2014. This produces the WN2 structure shown in Figure 5f.

The phases of WN1–WN4 in the northern polar region for each year produce the relatively zonally asymmetric variation. In contrast, in the southern polar region the phase of WN1 and WN2 is relatively stable and is almost independent year to year. This produces the persistent longitudinal variations in the southern polar region.

4. Discussion

Our discussion focuses on the influences of temperature and water vapor on the persistent longitudinal variations in the PMC albedo. The temperature data are from MLS/Aura and SABER/TIMED. The water vapor data are from MLS/Aura.

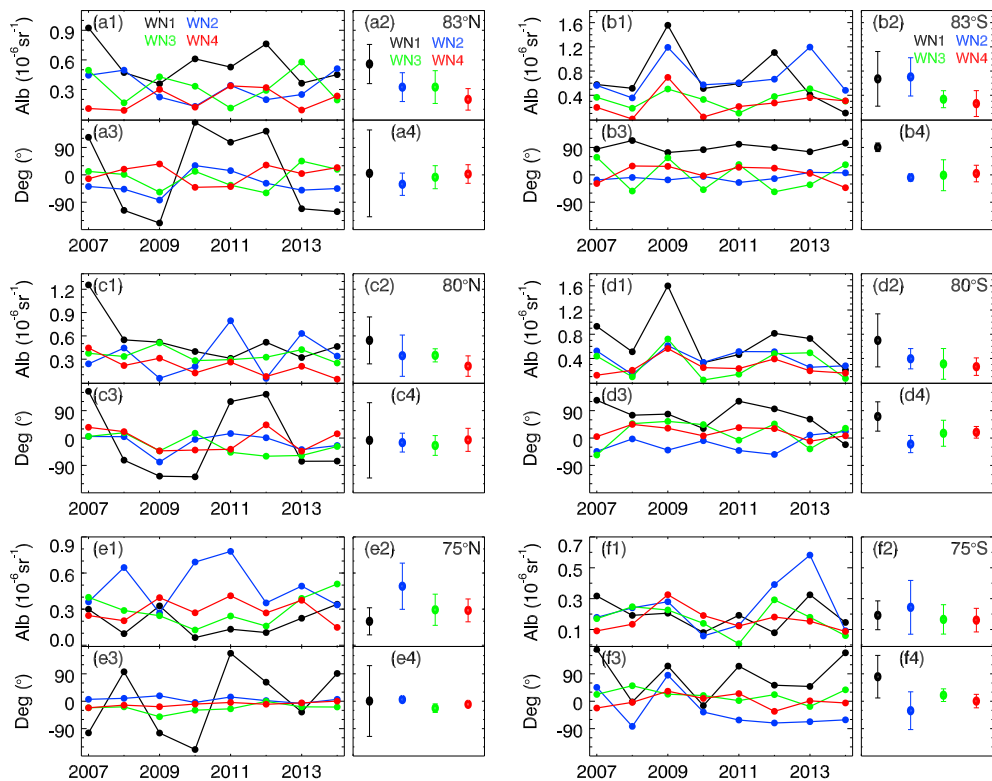


Figure 6. Amplitudes (upper two plots of each panel) and phases (lower two plots of each panel) of the WN1–WN4 (with different colors) of the PMC seasonal averaged albedo (left two plots of each panel) and their eight PMC seasons averages (right two plots of each panel, the error bars are the standard deviations of the amplitude of each wave number over the eight PMC seasons) at latitudes of 83°N/S, 80°N/S, and 75°N/S over the (b, d, and f) southern and (a, c, and e) northern polar regions from 2007 to 2014. The phase is defined as the longitude at which the peak of each wave number locates. The positive and negative degrees represent the east and west longitude, respectively.

4.1. Longitudinal Variations of MLS Temperature and H₂O and the Model Ice Mass Density

In this subsection, we show how the MLS/Aura temperature and H₂O at the PMC layer in the northern and southern polar regions can be used as inputs to the zero-dimensional (0-D) model (see Appendix A) developed by Hervig *et al.* [2009] to estimate the ice mass density in the PMC layers. The ice mass plays a fundamental role in determining the PMC albedo [Lumpe *et al.*, 2013] and thus can be used as an index of the simulated PMC albedo.

Figure 7 shows eight PMC seasons' averages of the normalized temperature, H₂O, and the derived ice mass density in the northern and southern polar regions, respectively. The ice mass density is calculated from the 0-D model with temperature and H₂O data from MLS/Aura at 0.0464 hPa (~84 km). The MLS temperature and H₂O data at ~84 km are used due to the following two reasons. First, the statistical results that the PMC peak heights are at 83.5 ± 1.7 km in NH and 84.7 ± 2.1 km in SH based on satellite and lidar observations [Chu *et al.*, 2006; Hervig *et al.*, 2013]. Second, the 0-D model is under the assumption that ice, local temperature, and water vapor are in the state of thermodynamic equilibrium. In this model the ice forms instantaneously from water vapor when the water vapor exceeds the value required for saturation [Hervig *et al.*, 2009]. The normalization process was performed using the same procedure as described in section 3.1. We note that the normalization process does not change the longitudinal pattern but eliminates the year-to-year variations. Consequently, the eight PMC seasons' averages of the normalized ice mass can be compared with the PMC albedo shown in Figure 4.

In the southern polar region at latitudes higher than 70°S, the normalized temperature is higher in the longitude range of 60°W to 150°W and lower in the longitude range of 30°E to 120°E than in other longitudes (Figure 7b). The normalized H₂O is rather low in the longitude range of 90°W to 140°E and is more abundant

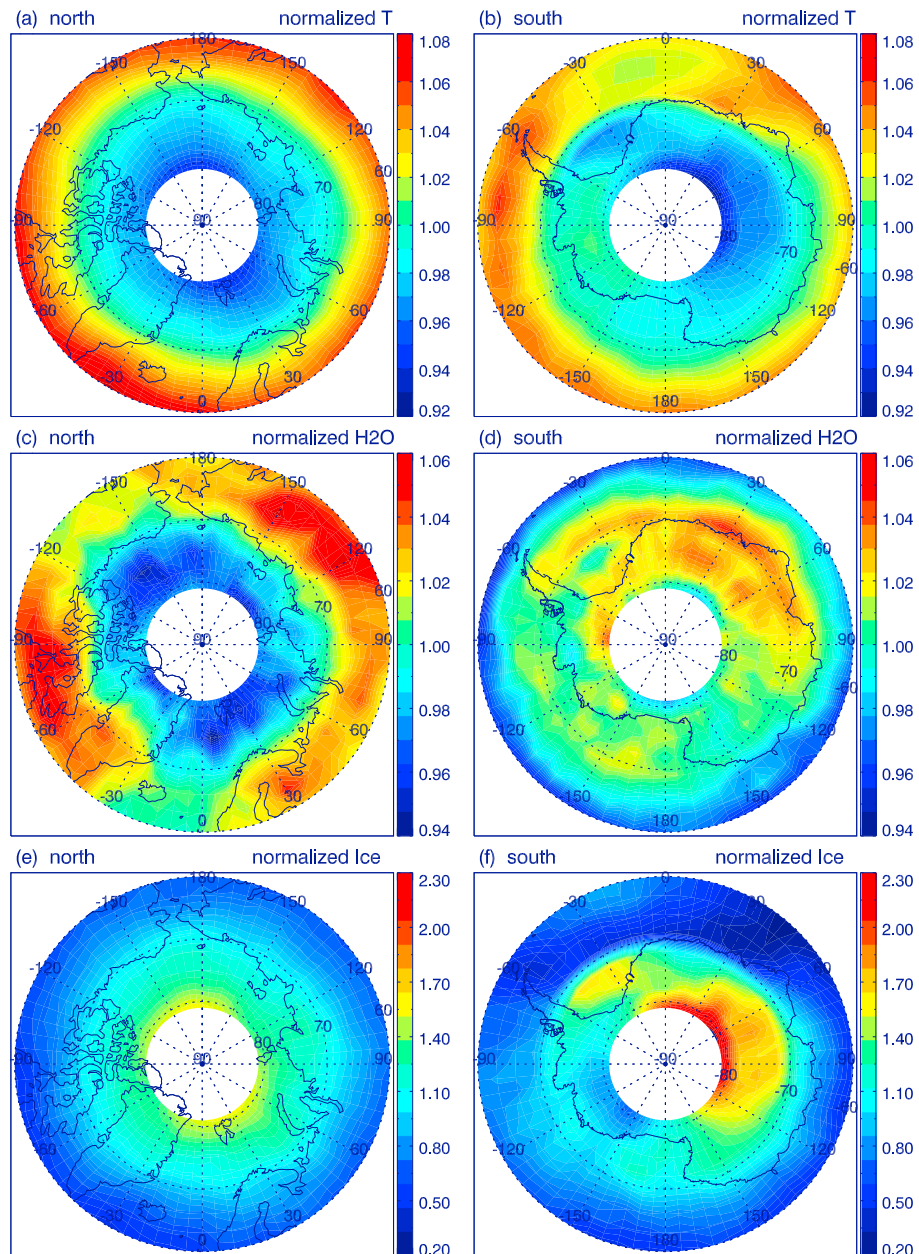


Figure 7. The eight PMC seasons (2007–2014) averages of the normalized (a, b) temperature and (c, d) H₂O observed by MLS/Aura and (e, f) the derived ice mass density using the O-D model with MLS/Aura temperature and H₂O as input in the (Figures 7a, 7c, and 7e) northern and (Figures 7b, 7d, and 7f) southern polar regions, respectively. The normalization process has been described in the text. The MLS data and ice mass are running averaged in the longitude direction with a window size of $\pm 7.5^\circ$ and step of 5.0° and then averaged in the latitudinal direction with a window size of 3° .

in the longitude range of 10°E to 80°E . The higher temperature and lower H₂O result in lower ice mass in the longitude range of 60°W to 150°W . In contrast, the lower temperature and higher amount of H₂O result in an abundant ice mass in the longitude range of 10°E to 120°E .

The ice mass exhibits larger fluctuations around its mean value in the southern polar region than those in the northern polar region (Figures 7e and 7f). The ice mass is more zonally asymmetric in the northern polar region and is consistent with the PMC albedo shown in Figure 4a. The longitudinal variations of ice mass in the southern polar region (weak in the longitude range of 60°W to 150°W and abundant in the longitude range of 10°E to 120°E) were consistent with the PMC albedo shown in Figure 4b.

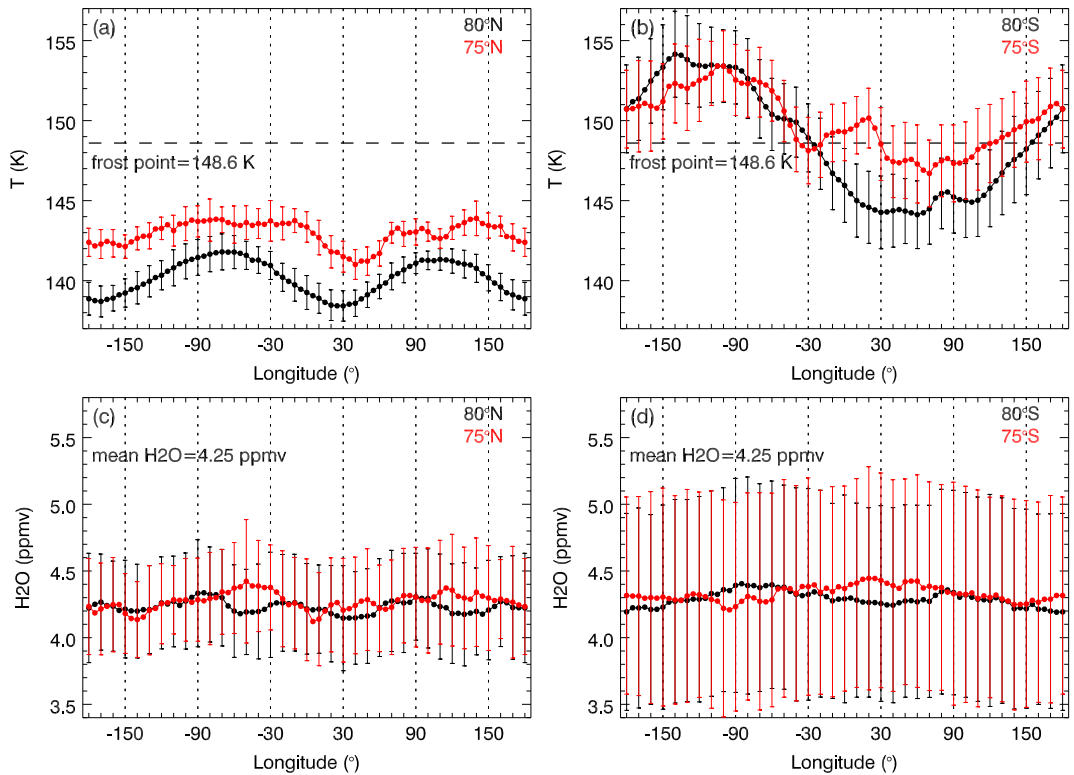


Figure 8. Longitudinal variations of MLS/Aura (a, b) temperature and (c, d) H_2O at 0.0464 hPa (~ 84 km) and then further averaged over the PMC seasons of 2007–2014 at 80°N/S (black) and 75°N/S (red), respectively. The running average is performed on longitude with a window size of $\pm 7.5^\circ$ and step of 5.0° . The latitude band used in the running average is 3° with centers at 80°N/S and 75°N/S, respectively. The error bars are the standard deviations when the temperature and H_2O averaged over the eight PMC seasons and indicate the PMC seasonal variability of temperature and H_2O , respectively.

It should be noted that there is a region of relatively higher ice mass in the longitude range of 10°W to 60°W and in the latitude band of 70°S to 75°S (Figure 7f). This agrees with the lower MLS/Aura temperature in this region (Figure 7b) but does not agree with the PMC albedo observation in the southern polar region shown in Figure 4b. The inconsistency between the ice mass and the CIPS PMC albedo might be a result that the PMC albedo imaged by CIPS is dependent on the particle size [McClintock *et al.*, 2009; Lumpe *et al.*, 2013]. In contrast, the ice mass density derived from 0-D model is a result from all the ice and does not depend on the particle size [Hervig *et al.*, 2009]. Moreover, the inconsistent might also be ascribed to the sampling at different LT (see sections 2.1 and 2.2) and coarse vertical resolution of MLS H_2O .

Comparisons of the patterns (regions having weak or strong perturbations) of ice mass, H_2O , and temperature showed that the ice mass is more strongly correlated with temperature than H_2O in the southern polar region. This indicates that temperature fluctuation is more important than H_2O in forming ice under certain environmental conditions. The importance of temperature fluctuations in forming ice depends on the mean temperature and H_2O content. If the mean temperature is far below the frost point, then the temperature fluctuation will not affect ice mass since all H_2O is already in an ice state. In contrast, if the mean temperature is near the frost point, then any fluctuation around the mean temperature would affect the formation of ice [Hervig *et al.*, 2009].

To illustrate the mean conditions of temperature and H_2O , we show the longitudinal variations of temperature and H_2O averaged over the eight PMC seasons at 80°N/S and 70°N/S in Figure 8. The error bars are the standard deviations (1σ) of temperature and H_2O when they averaged over the eight PMC seasons and indicate the PMC seasonal variability of temperature and H_2O . Both the temperature and H_2O exhibit larger PMC seasonal variability in the southern polar region than in the northern polar region (indicated by error bars) at all longitudes and all the time. The H_2O content is about 4 ppmv to 4.5 ppmv in both polar regions. Then the frost point is about 149 K according to the 0-D model. The mean temperature in the northern polar region is

below the frost point (Figure 8a). While the mean temperature in the southern polar region is near the frost point (Figure 8b). At some longitudes the temperature exceeds the frost point and at others it does not in the southern polar region. Thus, the temperature plays a more important role in controlling the ice mass in the southern polar region than in the northern polar region. Consequently, the ice mass follows the temperature more closely in the southern polar region than that in the northern polar region. This is consistent with the result of *Hervig et al.* [2015], who showed that PMC variability in the southern polar region is primarily controlled by temperature, while a combination of temperature and water vapor is responsible for the PMC variability in the northern polar region.

The eight PMC seasons' average temperature is higher in the Western Hemisphere than in the Eastern Hemisphere in the southern polar region (Figure 8b). This is also consistent with the weaker PMC albedo in the longitude range of 60°W to 150°W (Figure 4b).

MLS/Aura temperature supports the longitudinal variation in the PMC albedo. This consistency indicates that temperature plays a critical role in forming PMC. Thus, the persistent longitudinal variation in the PMC albedo is likely caused by the nonmigrating tides in temperature. However, the AIM satellite orbit is Sun-synchronous and the measurement was carried out at fixed local times. This will be explored using the SABER temperature, which has enough LT and longitude coverage, in section 4.2.

4.2. Nonmigrating Tides Derived From SABER Temperature

The SABER measurement covers only part of a PMC season, from the middle of May to the middle of June in the northern polar region and from the middle of November to January of the following year in the southern polar region [*Merkel et al.*, 2008]. There are 15 longitudes sampled at each LT corresponding to the ascending and descending nodes. We first bin the SABER temperatures over each PMC season into a composite day (bin temperatures in LT). The LT coverage is from 15 LT to 09 LT of the next day at 80°N/S and from 14 LT to 10 LT of the next day at 70°N/S [*Zhu et al.*, 2005]. Despite the fact that there are some missing data around noon, the SABER temperature can still be used to extract nonmigrating tides. Thus, we can explore the possible relations between the persistent longitudinal variations in PMC albedo and nonmigrating tides in temperature.

Forbes et al. [2003] and *Xu et al.* [2007, 2009, 2014] described the method of extracting the zonal mean and tides from SABER temperature data. Appendix B presents a brief description of the method. After removing the zonal mean and migrating tides with periods of 24, 12, 8, 6, 4.8, and 4 h from SABER temperature, we determine the residuals, which are mainly composed of nonmigrating tides. To compare with the eight PMC seasons' averages of PMC albedo shown in Figure 4, we show in Figure 9 the eight PMC seasons' averages of the residuals at 80°N/S and 75°N/S.

The residuals at 80°N and 75°N (Figures 9a and 9c) show that there is no apparent periodic signal either in LT or in longitude. This indicates that (1) there is no strong nonmigrating tide in each PMC season or (2) the phases of different nonmigrating tides vary from year to year and thus cancelled out the nonmigrating tides when they were averaged over the eight PMC seasons. To clarify the nonmigrating tides at 80°N and 75°N, we show in Figure 10 the seasonal averages of the longitude-LT distributions of the residuals at (from left to right) 80°N/S and 75°N/S from (from upper to below) 2007 to 2014. From the residual shown in Figure 10, we can see that there is no strong nonmigrating tide in each PMC season at 80°N and 75°N.

In contrast to the residuals at 80°N and 75°N, the residuals at 80°S and 75°S illustrate that there are apparent nonmigrating semidiurnal tides with zonal wave number 2 (Figures 9b and 9d). To make the nonmigrating semidiurnal tides in Figures 9b and 9d more readable, we overplotted red (blue) parallel lines to highlight warm (cold) phases. The warm (cold) phase means the constant line of maximum (minimum) temperature. The structure of zonal wave number 2 (WN2) in the longitude-LT frame, i.e., increasing in phase with increasing longitude with a rate of 12 h LT per 180° longitude, could be the mode of S0 (standing mode) in the longitude-UT frame. These nonmigrating semidiurnal tides are eight PMC seasons' average and cannot indicate that there are stable nonmigrating semidiurnal tides at 80°S and 75°S during these seasons. This can be illustrated with the residuals of each PMC season shown Figure 10. From Figure 10 we can see that the warm (highlighted by red lines) and cold (highlighted by blue lines) phases in each season do not vary from one season to another at 80°S and 75°S. The stable warm phases (from 0 to 12 LT, which is the LT coverage of CIPS in SH) during these seasons in SH West Hemisphere supports the weak albedo in the longitude range of 60°W–150°W over the southern polar region (see the seasonal averaged PMC albedo shown in Figure 2).

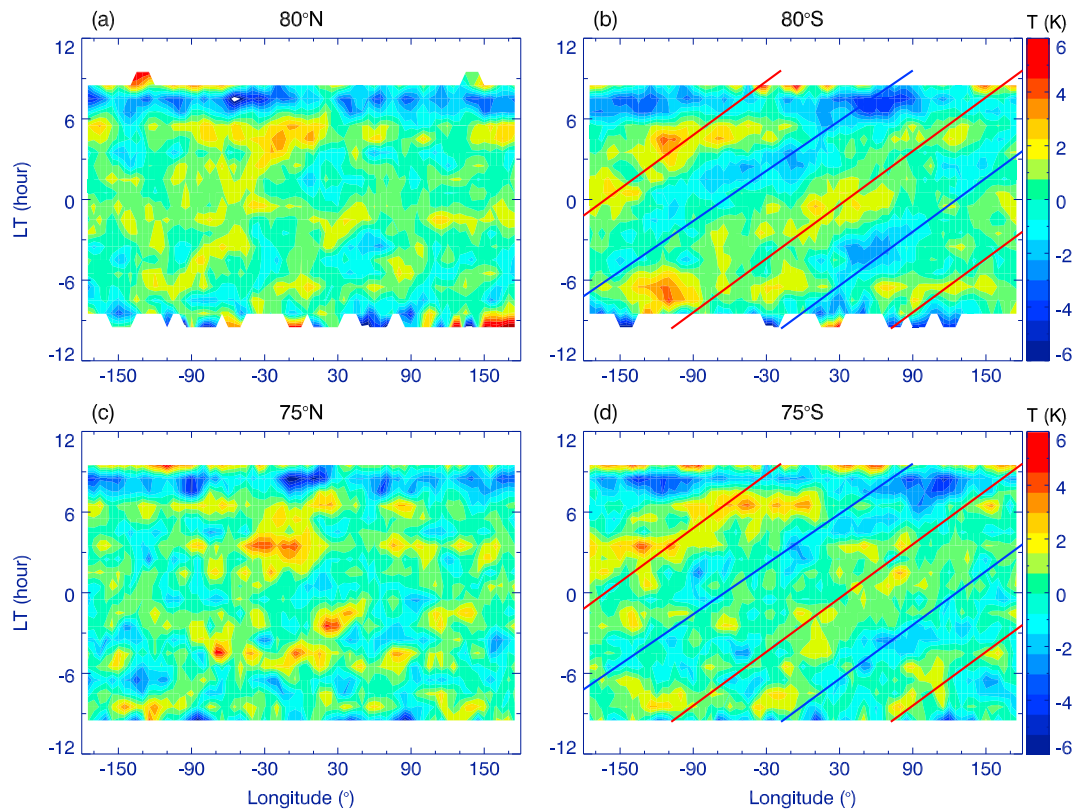


Figure 9. The eight seasons averages of the longitude-LT distributions of the residuals, which are defined as the SABER temperature after removing the zonal mean and migrating tides with periods of 24, 12, 8, 6, 4.8, and 4 h, at (from upper to below) 80°N/S and 75°N/S. The residuals in the SH are overplotted by red (blue) lines to highlight warm (cold) phases. Note that these lines are parallel with each other.

Consequently, the superposition of the residuals over the eight seasons produces regular warm and cold phases at 80°S and 75°S shown in Figures 9b and 9d. Moreover, the warm phase of the S0 mode is in the Western Hemisphere (especially in the longitude range of 30°W to 150°W) in the 0 LT–12 LT, which is also the LT coverage of CIPS in the southern polar region. Thus, the LT and longitude range of the warm phases of the S0 mode is consistent with the region of the low PMC albedo shown in Figure 4b and WN1 mode shown in Figure 5e. Moreover at 75°S, there are high temperatures patched on the cold phase of the residuals (Figure 11d). These high temperature patches might coincide with the WN2 mode shown in Figure 5f.

In Figure 11 we show the amplitudes of each tidal zonal wave number. The prominent modes are the semi-diurnal S0 at 80°N and SE2 at 75°N and terdiurnal TW1 at 80°N and SE1 at 75°N. In the southern polar region, the prominent modes are the semidiurnal S0 and SW1 at 80°S and S0, SE1, and SW1 at 75°S. There are also prominent terdiurnal tides with modes of TW1 at 80°S and TW2 at 75°S. In summary, the nonmigrating semidiurnal temperature tides with modes of S0, SW1, and SE1 are stronger in the southern polar region than those in the northern polar region.

Previous studies of winds observed by the radar network showed the presence of prominent nonmigrating semidiurnal tides with mode SW1 in the Antarctic MLT region [Murphy *et al.*, 2003, 2006, 2009]. Moreover, the winds observed by the TIMED Doppler Interferometer (TIDI) also indicated the existence of the nonmigrating semidiurnal tides with modes of SW1, SW3, S0, and SE1 in the Antarctic and with modes of SW1, SW3, and S0 in the Arctic [Iimura *et al.*, 2009, 2010]. In contrast, the nonmigrating semidiurnal tides of the above modes were much weaker in the Arctic summer than those in the Antarctic summer [Iimura *et al.*, 2010]. Our results on the nonmigrating semidiurnal tidal modes are consistent with those from radar network [Murphy *et al.*, 2003, 2006, 2009] and the hemispheric difference of the nonmigrating semidiurnal tides in wind revealed from TIDI [Iimura *et al.*, 2009, 2010]. Thus, it is reasonable to speculate that the low PMC albedo in the

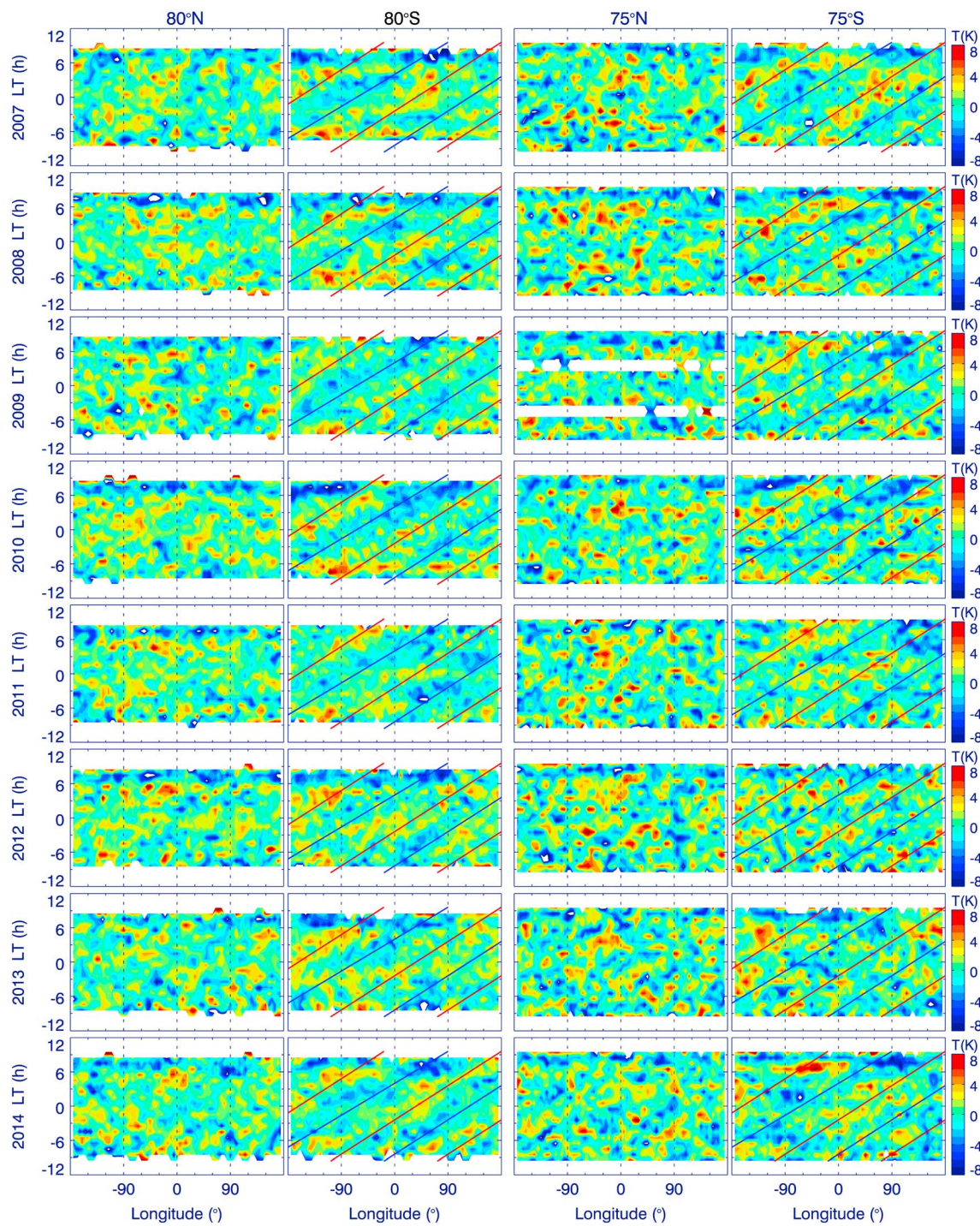


Figure 10. Seasonal averages of the longitude-LT distributions of the residuals, which are defined as the SABER temperature after removing the zonal mean and migrating tides with periods of 24, 12, 8, 6, 4.8, and 4 h, at (from left to right) 80°N/S and 75°N/S from (from upper to below) 2007 to 2014. The residuals in the SH are overplotted by red (blue) lines to highlight warm (cold) phases. Note that these lines are parallel with each other.

longitude range of 60°W to 150°W could be induced by the nonmigrating semidiurnal temperature tides with modes of S0, W1, and E1 in the southern polar region.

For the nonmigrating semidiurnal tides in the summertime polar region, both observations and simulation studies have suggested that they are likely generated by a nonlinear interaction between the migrating

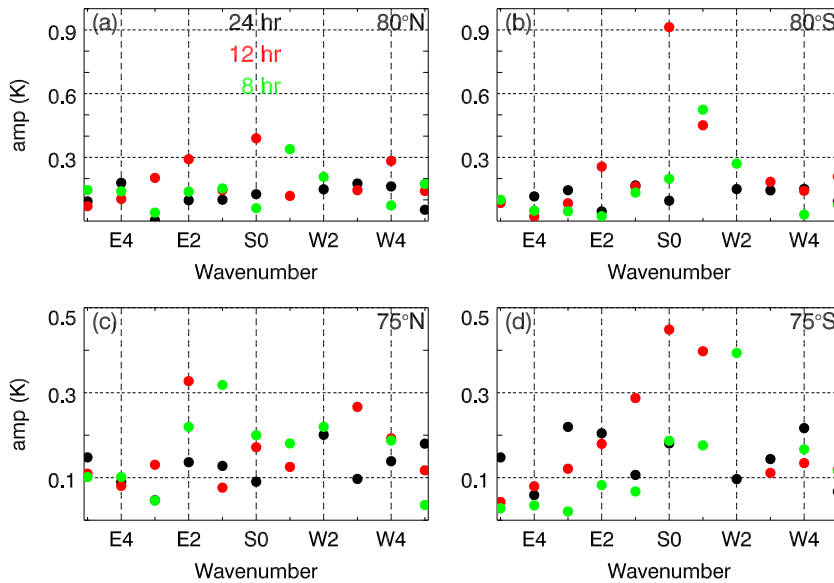


Figure 11. Amplitudes (a1, b1, c1, and d1) and phases (a2, b2, c2, and d2) of the nonmigrating tides with periods of 24 h (black), 12 h (red), and 8 h (green) derived from the residuals at 80°N/S (a1, a2, b1, and b2) and 75°N/S (c1, c2, d1, and d2) shown in Figure 10.

semidiurnal tide and quasi-stationary planetary waves (wave numbers 1 and 2) in the winter hemisphere that propagate across the equator to the summer hemisphere [Angelats i Coll and Forbes, 2002; Yamashita *et al.*, 2002; Smith *et al.*, 2007; Murphy *et al.*, 2009; Hibbins *et al.*, 2010]. Future studies will be carried out to determine the specific sources of the nonmigrating tides mentioned in this paper.

5. Summary and Conclusions

We analyzed the PMC albedo imaged by the CIPS/AIM instrument over the past eight PMC seasons (2007–2014) in the northern and southern polar regions. The 10 days averaged PMC albedo, seasonal averaged PMC albedo, and the PMC albedo averaged over eight PMC seasons are always low (~65% of the rest of the hemisphere) in the longitude range of 60°W to 150°W in the southern polar region. This persistent longitudinal variation in PMC albedo does not occur in the northern polar region.

Harmonic analyses of the longitudinal variations of the PMC albedo eight seasons average illustrate that the relative magnitudes of PMC albedo zonal wave numbers are latitude dependent. WN1 is prominent at 83°N/S and 80°N/S, and WN2 is prominent at 75°N/S. The low PMC albedo in the southern polar region is a result of the superposition of WN1 through WN4, since all of four wave numbers have minima in the longitude range of 60°W to 150°W and have stable phases over the eight PMC seasons at 83°S and 80°S. In the northern polar region, the amplitudes of WN1 through WN4 are smaller. Moreover, WN1 through WN4 minima are not exactly in the same longitude range and exhibit large year-to-year variability, and thus, no region of lower PMC albedo is formed.

The influences of temperature and H₂O on the persistent longitudinal variations of PMC albedo were discussed with the help of a 0-D PMC model, using temperature from MLS/Aura and SABER/TIMED and H₂O from MLS/Aura. After inputting the MLS temperature and H₂O into a 0-D PMC model, the resulting ice mass is more zonally asymmetric in the northern polar region than that in the southern polar region. In the southern polar region, the area of simulated low ice mass was generally consistent with the region of weak PMC albedo derived from CIPS.

Tidal analyses of the SABER temperature over the eight PMC seasons illustrated that there are substantial nonmigrating semidiurnal tides with modes of S0, SE1, and SW1 in the southern polar region. The warm phases of the S0, SW1, and SE1 modes were in the Western Hemisphere, which was consistent with the region of low PMC albedo. On the other hand, there is no strong nonmigrating tide in the northern polar

region. Thus, the prominent nonmigrating semidiurnal tides are likely to cause the persistent longitudinal variation in the PMC albedo in the southern polar region.

Appendix A: 0-D PMC Model

Hervig et al. [2009] developed a zero-dimensional (0-D) PMC model under the assumption that ice, local temperature, and water vapor are in the state of thermodynamic equilibrium. In this model the ice forms instantaneously from water vapor when the water vapor exceeds the value required for saturation. The basic formulae used in the model are summarized here. First, the saturation mixing ratio for water vapor ($P_{\text{H}_2\text{O}_{\text{sat}}}$, ppmv) adopted from *Murphy and Koop* [2005], is written as

$$P_{\text{H}_2\text{O}_{\text{sat}}} = \frac{10^6}{100(\text{hPa}) \cdot P} e^{9.550426 - \frac{5723.265}{T} + 3.53068 \cdot \log(T) - 0.00728332T}. \quad (\text{A1})$$

The saturation mixing ratio is dependent on temperature (T) and pressure (P). The 0-D model for ice mass density (ng/m^3) is written as

$$m_{\text{ice}} = \frac{10^9 \cdot (P_{\text{H}_2\text{O}} - P_{\text{H}_2\text{O}_{\text{sat}}}) \cdot P \cdot 10^2 \cdot 10^{-6}}{RT} M_{WW}. \quad (\text{A2})$$

Here the water vapor mixing ratio ($P_{\text{H}_2\text{O}}$) is an input parameter; $M_{WW} = 18.0 \text{ g/mol}$ is the molecular weight of H_2O , and $R = 8.314 \text{ J/(mol K)}$ is the gas constant. *Hervig et al.* [2009] developed a code for this model, which can be accessed from <http://gwest.gats-inc.com/software>. *Hervig et al.* [2009] showed that there was good agreement between the modeled and observed mixing ratios contained in the ice mass density. Recent studies by *Rong et al.* [2012, 2014] and *Russell et al.* [2014] showed also that the 0-D model is highly effective in reproducing ice mass density and daily PMC frequency.

Appendix B: Zonal Mean, Migrating, and Nonmigrating Tides

Following *Forbes et al.* [2003] and *Xu et al.* [2007, 2009, 2014], the zonal mean, migrating, and nonmigrating tides are obtained starting with the expression for temperature at the latitude ϕ and the altitude z as

$$T(t, \lambda) = \bar{T} + \sum_n \sum_s A_{n,s} \cos(n\Omega t + s\lambda - \phi_{n,s}). \quad (\text{B1})$$

By replacing the UT (t) to LT (t_{LT}) in Equation (B1), we get

$$T(t, \lambda) = \bar{T} + \sum_n \sum_s A_{n,s} \cos \left[2\pi \left(n \frac{t_{\text{LT}}}{24 \text{ hr}} + (s-n) \frac{\lambda}{360^\circ} \right) - \phi_{n,s} \right]. \quad (\text{B2})$$

Here $\Omega = 2\pi/(1 \text{ day})$ is the rotation rate of earth and λ is longitude (in degrees). The three terms on the right-hand side of equation (B1) are the zonal mean and the tides, including migrating ($s=n$) and nonmigrating ($s \neq n$) tides. $A_{n,s}$ and $\phi_{n,s}$ are, respectively, the amplitudes and phases of tides with periods of $24/n$ hour ($n=1$ for diurnal, $n=2$ for semidiurnal, $n=3$ for terdiurnal, etc.) and zonal wave numbers of s ($= -8, \dots, -3, -2, -1, 0, 1, 2, 3, \dots, 8$). Eastward (westward) propagating waves correspond to $s < 0$ ($s > 0$). The phases of the tides were defined as the longitude of maximum at $t=0$.

Before extracting these waves, we averaged the SABER temperature in the PMC layers (81 km–87 km) and performed a running average to get the temperature distribution as a function of longitude and LT. Thus, the SABER temperature in each PMC season is binned into a composite day (bin temperature in LT) by its running average. The running average is performed at longitude intervals with a window size of $\pm 7.5^\circ$ and step of 5.0° and on LT increments with a window size of $\pm 0.5 \text{ h}$ and step of 1 h , respectively. Figure B1a shows the longitude-LT contour of SABER temperature in the 2009 PMC season at 80°S . It can be seen that the LT gap is almost 8 h with its center at noon. The gap should be viewed with caution since it might alias the extracted zonal mean and wave signals.

Due to the LT gap, we extracted different waves step by step. First, the zonal mean and migrating tides (Figure B1b) with periods of 24, 12, 8, 6, 4.8, and 4 h are extracted and then removed from the observational data. The residuals (Figure B1c) are mainly composed of nonmigrating tides, planetary waves, and migrating tides with periods shorter than 4 h. Second, the nonmigrating tides are extracted from the residuals. The

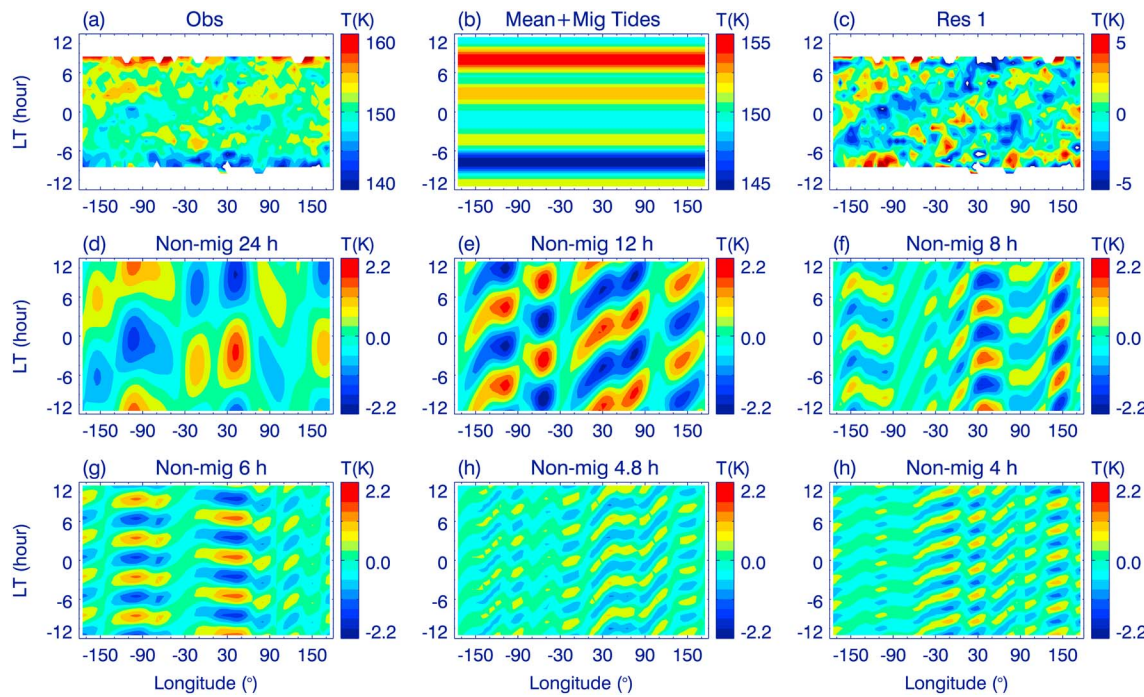


Figure B1. (a) SABER temperature in PMC season of 2009 is binned into one day by running averaging at a latitude band of 5° with center of 80°S . The running average is performed on longitude with a window size of $\pm 7.5^{\circ}$ and step of 5.0° and on LT with a window size of $\pm 0.5\text{ h}$ and step of 1 h ; (b) longitudinal-LT contours of zonal mean and migrating tides with periods of 24, 12, 8, 6, 4.8, and 4 h. (c) The residuals of the SABER temperature after removing the zonal mean and migrating tides. (d–h) The nonmigrating tides extracted from the residuals shown in Figure B1c with zonal wave numbers from -8 to 8 and with periods of 24, 12, 8, 6, 4.8, and 4 h, respectively.

nonmigrating tides with zonal wave numbers from -8 to 8 and with periods of 24, 12, 8, 6, 4.8, and 4 h are shown in Figures B1d through B1h, respectively.

A prominent feature in Figure B1 is that the residuals shown in Figure B1c exhibit a strong semidiurnal nonmigrating tide with a westward zonal wave number 2. This is the S0 mode of the semidiurnal nonmigrating tide as revealed from the horizontal winds observed by the ground-based radar network [Murphy *et al.*, 2006] and satellite data [Iimura *et al.*, 2009] in the Antarctic MLT region.

Acknowledgments

We thank the AIM/CIPS (<http://lasp.colorado.edu/aim/>), SABER (<ftp://saber.gats-inc.com/>), and MLS/Aura (<http://avdc.gsfc.nasa.gov/pub/data/satellite/Aura/MLS/V03/L2GP/>) data processing teams for providing the data used in this study. The 0-D model was downloaded from <http://gwest.gats-inc.com/> software. This work was supported by the Chinese Academy of Sciences (KZZD-EW-01-2), the National Science Foundation of China (41374158, 41574143, 41229001, and 41331069), the Educational Commission of Henan Province of China (17HASTIT010, 2014GGJS-047) and the Excellent Young Teachers of Henan Normal University (2014YQ0006), and the National Important Basic Research Project (grant 2011CB811405). This work was also supported in part by the Specialized Research Fund and the Open Research Program of the State Key Laboratory of Space Weather. The computations were supported by the High Performance Computing Center of Henan Normal University, Numerical Forecast Modeling R&D and VR System of State Key Lab. of Space Weather and Special HPC work stand of the Chinese Meridian Project.

References

- Angelats i Coll, M., and J. M. Forbes (2002), Nonlinear interactions in the upper atmosphere: The $s = 1$ and $s = 3$ nonmigrating semidiurnal tides, *J. Geophys. Res.*, **107**(A8), 1157, doi:10.1029/2001JA900179.
- Bailey, S. M., G. E. Thomas, D. W. Rusch, A. W. Merkel, C. D. Jeppesen, J. N. Carstens, C. E. Randall, W. E. McClintock, and J. M. Russell III (2009), Phase functions of polar mesospheric cloud ice as observed by the CIPS instrument on the AIM satellite, *J. Atmos. Sol. Terr. Phys.*, **71**, 373–380, doi:10.1016/j.jastp.2008.09.039.
- Benze, S., C. E. Randall, B. Karlsson, V. L. Harvey, M. T. DeLand, G. E. Thomas, and E. P. Shettle (2012), On the onset of polar mesospheric cloud seasons as observed by SBUV, *J. Geophys. Res.*, **117**, D07104, doi:10.1029/2011JD017350.
- Chandran, A., D. W. Rusch, A. W. Merkel, S. E. Palo, G. E. Thomas, M. J. Taylor, S. M. Bailey, and J. M. Russell III (2010), Polar mesospheric cloud structures observed from the cloud imaging and particle size experiment on the Aeronomy of Ice in the Mesosphere spacecraft: Atmospheric gravity waves as drivers for longitudinal variability in polar mesospheric cloud occurrence, *J. Geophys. Res.*, **115**, D13102, doi:10.1029/2009JD013185.
- Chandran, A., D. W. Rusch, G. E. Thomas, S. E. Palo, G. Baumgarten, E. J. Jensen, and A. W. Merkel (2012), Atmospheric gravity wave effects on polar mesospheric clouds: A comparison of numerical simulations from CARMA 2D with AIM observations, *J. Geophys. Res.*, **117**, D20104, doi:10.1029/2012JD017794.
- Chu, X., C. S. Gardner, and R. G. Roble (2003), Lidar studies of interannual, seasonal, and diurnal variations of polar mesospheric clouds at the South Pole, *J. Geophys. Res.*, **108**(D8), 8447, doi:10.1029/2002JD002524.
- Chu, X., P. J. Espy, G. J. Nott, J. C. Dietrich, and C. S. Gardner (2006), Polar mesospheric clouds observed by an iron Boltzmann lidar at Rothera (67.51°S , 68.01°W), Antarctica from 2002 to 2005: Properties and implications, *J. Geophys. Res.*, **111**, D20213, doi:10.1029/2006JD007086.
- Chu, X., C. Yamashita, P. J. Espy, G. J. Nott, E. J. Jensen, H. L. Liu, W. Huang, and J. P. Thayer (2009), Responses of polar mesospheric cloud brightness to stratospheric gravity waves at the South Pole and Rothera, Antarctica, *J. Atmos. Sol. Terr. Phys.*, **71**, 434–445, doi:10.1016/j.jastp.2008.10.002.
- DeLand, M. T., and G. E. Thomas (2015), Updated PMC trends derived from SBUV data, *J. Geophys. Res. Atmos.*, **120**, 2140–2166, doi:10.1002/2014JD022253.
- DeLand, M. T., E. P. Shettle, G. E. Thomas, and J. J. Olivero (2007), Latitude-dependent long-term variations in polar mesospheric clouds from SBUV version 3 PMC data, *J. Geophys. Res.*, **112**, D10315, doi:10.1029/2006JD007857.

- DeLand, M. T., E. P. Shettle, G. E. Thomas, and J. J. Olivero (2011), Direct observations of PMC local time variations by Aura OMI, *J. Atmos. Sol. Terr. Phys.*, 73, 2049–2064, doi:10.1016/j.jastp.2010.11.019.
- Fiedler, J., G. Baumgarten, and G. von Cossart (2005), Mean diurnal variations of noctilucent clouds during 7 years of lidar observations at ALOMAR, *Ann. Geophys.*, 23, 1175–1181, doi:10.5194/angeo-23-1175-2005.
- Fiedler, J., G. Baumgarten, U. Berger, P. Hoffmann, N. Kaifler, and F.-J. Lübben (2011), NLC and the background atmosphere above ALOMAR, *Atmos. Chem. Phys.*, 11, 5701–5717, doi:10.5194/acp-11-5701-2011.
- Forbes, J. M., X. Zhang, E. R. Talaat, and W. Ward (2003), Nonmigrating diurnal tides in the thermosphere, *J. Geophys. Res.*, 108(A1), 1033, doi:10.1029/2002JA009262.
- Gerrard, A. J., T. J. Kane, and J. P. Thayer (1998), Noctilucent clouds and wave dynamics: Observations at Sondrestrom, Greenland, *Geophys. Res. Lett.*, 25(15), 2817–2820, doi:10.1029/98GL02107.
- Gerrard, A., J. Thayer, and T. Kane (2002), Mesospheric clouds and the duality of gravity waves, *Eos Trans. AGU*, 83(43), 488, doi:10.1029/2002EO000344.
- Hervig, M. E., R. E. Thompson, M. E. McHugh, L. L. Gordley, J. M. Russell III, and M. E. Summers (2001), First confirmation that water ice is the primary component of polar mesospheric clouds, *Geophys. Res. Lett.*, 28, 971–974, doi:10.1029/2000GL012104.
- Hervig, M. E., M. H. Stevens, L. L. Gordley, L. E. Deaver, J. M. Russell III, and S. Bailey (2009), Relationships between PMCs, temperature and water vapor from SOFIE observations, *J. Geophys. Res.*, 114, D20203, doi:10.1029/2009JD012302.
- Hervig, M. E., D. E. Siskind, M. H. Stevens, and L. E. Deaver (2013), Interhemispheric comparison of PMCs and their environment from SOFIE observations, *J. Atmos. Sol. Terr. Phys.*, 104, 285–298, doi:10.1016/j.jastp.2012.10.013.
- Hervig, M. E., D. E. Siskind, S. M. Bailey, and J. M. Russell III (2015), The influence of PMCs on water vapor and drivers behind PMC variability from SOFIE observations, *J. Atmos. Sol. Terr. Phys.*, 132, 124–134, doi:10.1016/j.jastp.2015.07.010.
- Hibbins, R. E., O. J. Marsh, A. J. McDonald, and M. J. Jarvis (2010), Interannual variability of the $S = 1$ and $S = 2$ components of the semidiurnal tide in the Antarctic MLT, *J. Atmos. Sol. Terr. Phys.*, 72, 794–800, doi:10.1016/j.jastp.2010.03.026.
- Imura, H., S. E. Palo, Q. Wu, T. L. Killeen, S. C. Solomon, and W. R. Skinner (2009), Structure of the nonmigrating semidiurnal tide above Antarctica observed from the TIMED Doppler Interferometer, *J. Geophys. Res.*, 114, D11102, doi:10.1029/2008JD010608.
- Imura, H., D. C. Fritts, Q. Wu, W. R. Skinner, and S. E. Palo (2010), Nonmigrating semidiurnal tide over the Arctic determined from TIMED Doppler Interferometer wind observations, *J. Geophys. Res.*, 115, D06109, doi:10.1029/2009JD012733.
- Innis, J., A. R. Klekociuk, R. J. Morris, A. Cunningham, A. Graham, and D. J. Murphy (2008), A study of the relationship between stratospheric gravity waves and polar mesospheric clouds at Davis, Antarctica, *J. Geophys. Res.*, 113, D14102, doi:10.1029/2007JD00931.
- Jensen, E., and G. E. Thomas (1988), A growth-sedimentation model of polar mesospheric clouds: Comparison with SME measurements, *J. Geophys. Res.*, 93(D3), 2461–2473, doi:10.1029/JD093iD03p02461.
- Jensen, E. J., and G. E. Thomas (1994), Numerical simulations of the effects of gravity waves on noctilucent clouds, *J. Geophys. Res.*, 99(D2), 3421–3430, doi:10.1029/93JD01736.
- Karlsson, B., and M. Rapp (2006), Latitudinal dependence of noctilucent cloud growth, *Geophys. Res. Lett.*, 33, L11812, doi:10.1029/2006GL025805.
- Karlsson, B., H. Körnich, and J. Gumbel (2007), Evidence for interhemispheric stratosphere-mesosphere coupling derived from noctilucent cloud properties, *Geophys. Res. Lett.*, 34, L16806, doi:10.1029/2007GL030282.
- Karlsson, B., C. E. Randall, S. Benze, M. Mills, V. L. Harvey, S. M. Bailey, and J. M. Russell III (2009), Intra-seasonal variability of polar mesospheric clouds due to inter-hemispheric coupling, *Geophys. Res. Lett.*, 36, L20802, doi:10.1029/2009GL040348.
- Kirkwood, S., V. Barabash, U. E. Brandstrom, A. Mostrom, K. Stebel, N. Mitchell, and W. Hocking (2002), Noctilucent clouds, PMSE and 5-day planetary waves: A case study, *Geophys. Res. Lett.*, 29(10), 1411, doi:10.1029/2001GL014022.
- Kirkwood, S., P. Dalin, and A. Réchou (2008), Noctilucent clouds observed from the UK and Denmark-Trends and variations over 43 years, *Ann. Geophys.*, 26, 1243–1254, doi:10.5194/angeo-26-1243-2008.
- Lambert, A., et al. (2007), Validation of the Aura Microwave Limb Sounder middle atmosphere water vapor and nitrous oxide measurements, *J. Geophys. Res.*, 112, D24S36, doi:10.1029/2007JD008724.
- Liu, X., J. Yue, J. Xu, L. Wang, W. Yuan, J. M. Russell III, and M. E. Hervig (2014), Gravity wave variations in the polar stratosphere and mesosphere from SOFIE/ AIM temperature observations, *J. Geophys. Res. Atmos.*, 119, 7368–7381, doi:10.1002/2013JD021439.
- Liu, X., J. Yue, J. Xu, W. Yuan, J. M. Russell III, and M. E. Hervig (2015), Five-day waves in polar stratosphere and mesosphere temperature and mesospheric ice water measured by SOFIE/ AIM, *J. Geophys. Res. Atmos.*, 120, 3872–3887, doi:10.1002/2015JD023119.
- Lübben, F.-J., J. Höffner, T. P. Viehl, B. Kaifler, and R. J. Morris (2011), First measurements of thermal tides in the summer mesopause region at Antarctic latitudes, *Geophys. Res. Lett.*, 38, L24806, doi:10.1029/2011GL050045.
- Lumpe, J., et al. (2013), Retrieval of polar mesospheric cloud properties from CIPS: Algorithm description, error analysis and cloud detection sensitivity, *J. Atmos. Sol. Terr. Phys.*, 104, 167–196, doi:10.1016/j.jastp.2013.06.007.
- McClintock, W., D. W. Rusch, G. E. Thomas, A. W. Merkel, M. R. Lankton, V. A. Drake, S. M. Bailey, and J. M. Russell III (2009), The cloud imaging and particle size experiment on the Aeronomy of Ice in the Mesosphere mission: Instrument concept, design, calibration, and on-orbit performance, *J. Atmos. Sol. Terr. Phys.*, 71, 340–355, doi:10.1016/j.jastp.2008.10.011.
- Merkel, A. W., G. E. Thomas, S. E. Palo, and S. M. Bailey (2003), Observations of the 5 day planetary wave in PMC measurements from the Student Nitric Oxide Explorer Satellite, *Geophys. Res. Lett.*, 30(4), 1196, doi:10.1029/2002GL016524.
- Merkel, A. W., R. R. Garcia, S. M. Bailey, and J. M. Russell III (2008), Observational studies of planetary waves in PMCs and mesospheric temperature measured by SNOE and SABER, *J. Geophys. Res.*, 113, D14202, doi:10.1029/2007JD009396.
- Murphy, D. J., M. Tsutsumi, D. M. Riggan, G. O. L. Jones, R. A. Vincent, M. E. Hagan, and S. K. Avery (2003), Observations of a nonmigrating component of the semidiurnal tide over Antarctica, *J. Geophys. Res.*, 108(D8), 4241, doi:10.1029/2002JD003077.
- Murphy, D. J., et al. (2006), A climatology of tides in the Antarctic mesosphere and lower thermosphere, *J. Geophys. Res.*, 111, D23104, doi:10.1029/2005JD006803.
- Murphy, D. J., T. Aso, D. C. Fritts, R. E. Hibbins, A. J. McDonald, D. M. Riggan, M. Tsutsumi, and R. A. Vincent (2009), Source regions for Antarctic MLT non-migrating semidiurnal tides, *Geophys. Res. Lett.*, 36, L09805, doi:10.1029/2008GL037064.
- Murphy, D. M., and T. Koop (2005), Review of the vapour pressure of ice and super-cooled water for atmospheric applications, *Q. J. R. Meteorol. Soc.*, 131, 1539–1565, doi:10.1256/qj.04.94.
- Nielsen, K., D. E. Siskind, S. D. Eckermann, K. W. Hoppel, L. Coy, J. P. McCormack, S. Benze, C. E. Randall, and M. E. Hervig (2010), Seasonal variation of the quasi 5 day planetary wave: Causes and consequences for polar mesospheric cloud variability in 2007, *J. Geophys. Res.*, 115, D18111, doi:10.1029/2009JD012676.
- Rapp, M., and G. E. Thomas (2006), Modeling the microphysics of mesospheric ice particles: Assessment of current capabilities and basic sensitivities, *J. Atmos. Sol. Terr. Phys.*, 68, 715–744, doi:10.1016/j.jastp.2005.10.015.

- Robert, C. E., C. von Savigny, N. Rahpoe, H. Bovensmann, J. P. Burrows, M. T. DeLand, and M. J. Schwartz (2010), First evidence of a 27 day solar signature in noctilucent cloud occurrence frequency, *J. Geophys. Res.*, 115, D00112, doi:10.1029/2009JD012359.
- Rong, P. P., J. M. Russell III, M. E. Hervig, and S. M. Bailey (2012), The roles of temperature and water vapor at different stages of the polar mesospheric cloud season, *J. Geophys. Res.*, 117, D04208, doi:10.1029/2011JD016464.
- Rong, P. P., J. M. Russell III, C. E. Randall, S. M. Bailey, and A. Lambert (2014), Northern PMC brightness zonal variability and its correlation with temperature and water vapor, *J. Geophys. Res. Atmos.*, 119, 2390–2408, doi:10.1002/2013JD020513.
- Rusch, D. W., G. E. Thomas, W. McClintock, A. W. Merkel, S. M. Bailey, J. M. Russell III, C. E. Randall, C. Jeppesen, and M. Callan (2009), The cloud imaging and particle size experiment on the aeronomy of ice in the mesosphere mission: Cloud morphology for the northern 2007 season, *J. Atmos. Sol. Terr. Phys.*, 71, 356–364, doi:10.1016/j.jastp.2008.11.005.
- Russell, J. M., III, M. G. Mlynczak, L. L. Gordley, J. Tansock, and R. Esplin (1999), An overview of the SABER experiment and preliminary calibration results, *Proc. SPIE Int. Soc. Opt. Eng.*, 3756, 277–288.
- Russell, J. M., III, et al. (2009), The Aeronomy of Ice in the Mesosphere (AIM) mission: Overview and early science results, *J. Atmos. Sol. Terr. Phys.*, 71, 289–299, doi:10.1016/j.jastp.2008.08.011.
- Russell, J. M., III, P. Rong, S. M. Bailey, M. E. Hervig, and S. V. Petelina (2010), Relationship between the summer mesopause and polar mesospheric cloud heights, *J. Geophys. Res.*, 115, D16209, doi:10.1029/2010JD013852.
- Russell, J. M., III, P. Rong, M. E. Hervig, D. E. Siskind, M. H. Stevens, S. M. Bailey, and J. Gumbel (2014), Analysis of northern midlatitude noctilucent cloud occurrences using satellite data and modeling, *J. Geophys. Res. Atmos.*, 119, 3238–3250, doi:10.1002/2013JD021017.
- Schoeberl, M. R., et al. (2006), Overview of the EOS Aura mission, *IEEE Trans. Geosci. Remote Sens.*, 44, 1066–1075.
- Schwartz, M. J., et al. (2008), Validation of the Aura Microwave Limb Sounder temperature and geopotential height measurements, *J. Geophys. Res.*, 113, D15S11, doi:10.1029/2007JD008783.
- Shettle, E. P., M. T. DeLand, G. E. Thomas, and J. J. Olivero (2009), Long-term variations in the frequency of polar mesospheric clouds in the Northern Hemisphere from SBUV, *Geophys. Res. Lett.*, 36, L02803, doi:10.1029/2008GL036048.
- Siskind, D. E., M. H. Stevens, and C. R. Englert (2005), A model study of global variability in mesospheric cloudiness, *J. Atmos. Sol. Terr. Phys.*, 63, 501–513, doi:10.1016/j.jastp.2004.11.007.
- Siskind, D. E., M. H. Stevens, M. Hervig, F. Sassi, K. Hoppel, C. R. Englert, and A. J. Kochenash (2011), Consequences of recent Southern Hemisphere winter variability on polar mesospheric clouds, *J. Atmos. Sol. Terr. Phys.*, 73, 2013–2021, doi:10.1016/j.jastp.2011.06.014.
- Smith, A. K., D. V. Pancheva, N. J. Mitchell, D. R. Marsh, J. M. Russell III, and M. G. Mlynczak (2007), A link between variability of the semidiurnal tide and planetary waves in the opposite hemisphere, *Geophys. Res. Lett.*, 34, L07809, doi:10.1029/2006GL028929.
- Stevens, M. H., C. R. Englert, M. T. DeLand, and S. M. Bailey (2007), Polar mesospheric cloud mass and the ice budget: 2. Application to satellite data sets, *J. Geophys. Res.*, 112, D08205, doi:10.1029/2006JD007532.
- Stevens, M. H., C. R. Englert, M. Hervig, S. V. Petelina, W. Singer, and K. Nielsen (2009), The diurnal variation of polar mesospheric cloud frequency near 55°N observed by SHIMMER, *J. Atmos. Sol. Terr. Phys.*, 71, 401–407, doi:10.1016/j.jastp.2008.10.009.
- Stevens, M. H., et al. (2010), Tidally induced variations of polar mesospheric cloud altitudes and ice water content using a data assimilation system, *J. Geophys. Res.*, 115, D18209, doi:10.1029/2009JD013225.
- Thayer, J. P., M. Rapp, A. J. Gerrard, E. Gudmundsson, and T. J. Kane (2003), Gravity wave influences on Arctic mesospheric clouds as determined by a Rayleigh lidar at Sondrestrom, Greenland, *J. Geophys. Res.*, 108(D8), 8449, doi:10.1029/2002JD002363.
- Thomas, G. E. (1996), Is the polar mesosphere the miner's canary of global change?, *Adv. Space Res.*, 18, 149–158, doi:10.1016/0273-1177(95)00855-9.
- Thomas, G. E. (2003), Are noctilucent clouds harbingers of global change in the middle atmosphere?, *Adv. Space Res.*, 32, 1737–1746, doi:10.1016/S0273-1177(03)90470-4.
- Thomas, G. E., J. J. Olivero, M. DeLand, and E. P. Shettle (2003), Comment on "Are noctilucent clouds truly a "Miner's Canary" for Global Change?", *Eos Trans. AGU*, 84(36), 352–353, doi:10.1029/2003EO360008.
- Thomas, G. E., B. Thuraiajah, M. E. Hervig, C. von Savigny, and M. Snow (2015), Solar-induced 27-day variations of mesospheric temperature and water vapor from the AIM SOFIE experiment: Drivers of polar mesospheric cloud variability, *J. Atmos. Sol. Terr. Phys.*, 134, 56–68, doi:10.1016/j.jastp.2015.09.015.
- von Savigny, C., C. Roberts, H. Bovensmann, J. P. Burrows, and M. Schwartz (2007), Satellite observations of the quasi 5 day wave in noctilucent clouds and mesopause temperatures, *Geophys. Res. Lett.*, 34, L24808, doi:10.1029/2007GL030987.
- Xu, J., A. K. Smith, W. Yuan, H.-L. Liu, Q. Wu, M. G. Mlynczak, and J. M. Russell III (2007), Global structure and long-term variations of zonal mean temperature observed by TIMED/SABER, *J. Geophys. Res.*, 112, D24106, doi:10.1029/2007JD008546.
- Xu, J., A. K. Smith, H.-L. Liu, W. Yuan, Q. Wu, G. Jiang, M. G. Mlynczak, J. M. Russell III, and S. J. Franke (2009), Seasonal and quasi-biennial variations in the migrating diurnal tide observed by Thermosphere, Ionosphere, Mesosphere, Energetics and Dynamics (TIMED), *J. Geophys. Res.*, 114, D13107, doi:10.1029/2008JD011298.
- Xu, J., A. K. Smith, M. Liu, X. Liu, H. Gao, G. Jiang, and W. Yuan (2014), Evidence for nonmigrating tides produced by the interaction between tides and stationary planetary waves in the stratosphere and lower mesosphere, *J. Geophys. Res. Atmos.*, 119, 471–489, doi:10.1002/2013JD020150.
- Yamashita, K., S. Miyahara, Y. Miyoshi, K. Kawano, and J. Ninomiya (2002), Seasonal variation of non-migrating semidiurnal tide in the polar MLT region in a general circulation model, *J. Atmos. Sol. Terr. Phys.*, 64, 1083–1094.
- Zhu, X., J.-H. Yee, E. R. Talaat, M. Mlynczak, L. Gordley, C. Mertens, and J. M. Russell III (2005), An algorithm for extracting zonal mean and migrating tidal fields in the middle atmosphere from satellite measurements: Applications to TIMED/SABER-measured temperature and tidal modeling, *J. Geophys. Res.*, 110, D02105, doi:10.1029/2004JD004996.